

Temperature Scaling Attack

Disrupting Model Confidence in Federated Learning

Kichang Lee Jaeho Jin
Yonsei University *Yonsei University*

JaeYeon Park Songkuk Kim JeongGil Ko
Dankook University *Yonsei University* *Yonsei University*

Abstract

Predictive confidence serves as a foundational control signal in mission-critical systems, directly governing risk-aware logic such as escalation, abstention, and conservative fallback. While prior federated learning attacks predominantly target accuracy or implant backdoors, we identify *confidence calibration* as a distinct attack objective. We present the *Temperature Scaling Attack (TSA)*, a training-time attack that degrades calibration while preserving accuracy. By injecting temperature scaling with learning rate-temperature coupling during local training, malicious updates maintain benign-like optimization behavior, evading accuracy-based monitoring and similarity-based detection. We provide a convergence analysis under non-IID settings, showing that this coupling preserves standard convergence bounds while systematically distorting confidence. Across three benchmarks, TSA substantially shifts calibration (e.g., 14% error increase on CIFAR-100) with <2% accuracy change, and remains effective under robust aggregation and post-hoc calibration defenses. Case studies further show that confidence manipulation can cause up to 7.2 \times increases in missed critical cases (healthcare) or false alarms (autonomous driving), even when accuracy is unchanged. Overall, our results establish calibration integrity as a critical attack surface in federated learning.

1 Introduction

Predictive confidence is a cornerstone of operational reliability in modern safety-critical systems [43]. In domains such as autonomous driving [2, 23], remote clinical monitoring [42], and industrial robotics [28], probability outputs are not merely explanatory; they are consumed as foundational control signals for risk-aware policies [25]. For example, a vehicle may engage conservative fallback behaviors when confidence is low, and a healthcare pipeline may escalate uncertain cases for human review [14]. These mechanisms implicitly assume *calibration*: a confidence score should correspond to the empirical likelihood of correctness [40]. When this alignment

is systematically distorted, over-confidence can suppress vital safeguards, while under-confidence can trigger excessive verification, degrading both safety and operational efficiency.

In many such systems, federated learning (FL) is increasingly adopted to reduce the need for centralizing sensitive user data while enabling personalization at scale. However, decentralization fundamentally enlarges the adversarial surface. Existing FL security research has largely remained accuracy-centric, focusing on poisoning attacks that disrupt convergence or backdoors that induce targeted misclassifications [3, 11, 48]. While effective at causing errors, these attacks can often be detectable in practice [5, 29, 30]; noticeable drops in validation accuracy or abnormal training dynamics serve as immediate red flags, triggering server-side auditing and mitigation.

For a sophisticated adversary, a more insidious threat is to preserve model utility while subverting its operational reliability [53]. By targeting to attack the calibration rather than accuracy, the attacker can keep the model deployable and continue to deliver seemingly correct predictions to end users, while systematically distorting the probability scale that downstream policies rely on [41]. This creates a silent failure mode, given that deployed systems typically monitor only accuracy or loss, as calibration assessment requires representative validation data that is rarely available post-deployment. Consequently, the system may pass standard accuracy-based validation while safety gating and triage logic driven by model confidence become systematically unreliable.

Such a risk is amplified in federated settings with inherently non-IID client data [36]. Post-hoc calibration is also challenging to apply: each client’s validation set is small, biased, and often mismatched to the global deployment distribution [9, 44]. As a result, local corrections are weakened and “normal” confidence behavior becomes ill-defined across clients and rounds, hindering reliable auditing of calibration manipulation.

The consequences of such silent calibration failures can be severe. In autonomous driving, an over-confident model may suppress critical safety fallbacks even when making incor-

rect predictions, directly increasing accident risk. In healthcare triage, systematic under-confidence can overwhelm clinicians with false alarms, degrading both efficiency and patient safety. Unlike accuracy-based attacks that trigger immediate red flags, calibration manipulation remains deployable while corrupting the signals that safety mechanisms depend on.

However, executing such confidence manipulation in FL presents unique technical challenges. FL servers typically employ robust aggregation rules and update-level anomaly detectors to filter malicious updates. At the same time, client updates are naturally heterogeneous under non-IID data, creating noise that can mask attack signatures. To remain evasive and persistent, an attacker must be *optimization-aware*, meaning that they must produce updates that strictly adhere to the expected global descent direction to avoid being flagged as outliers, while systematically distorting the model’s logit distributions to reshape its confidence.

To address these challenges, we introduce the ***Temperature Scaling Attack (TSA)***, a training-time mechanism that selectively degrades calibration in federated learning without materially affecting predictive accuracy. Guided by a non-convex convergence analysis under heterogeneous (non-IID) client data, we show that coupling temperature with the learning rate preserves a constant effective step size, stabilizing optimization while systematically shifting model confidence.

Across three benchmarks, TSA induces substantial calibration degradation while keeping accuracy within $\pm 1\text{-}2\%$ of baseline. For instance, on CIFAR-100, TSA shifts the model from moderately to severely over-confident (calibration error +145%) while changing accuracy by less than 2%. We further provide a multi-view analysis (convergence, parameter-space similarity, and representation-space similarity) showing that TSA bypasses common server-side audits. Malicious updates closely mimic benign optimization, remaining highly similar to clean gradients and representations and thus evading detectors that readily flag conventional poisoning.

We further evaluate TSA against existing defenses and show that the attack persists under byzantine-robust aggregation rules and post-hoc calibration procedures. Finally, we validate real-world relevance through three case studies. In mobile healthcare triage, confidence manipulation causes up to $7.2\times$ increase in missed critical cases (over-confidence) or unnecessary clinician reviews (under-confidence). In autonomous driving, miscalibration leads to detection failures that either miss objects entirely or flood the pipeline with false alarms. For language generation, degraded probability estimates corrupt decoding logic, producing repetitive and factually inconsistent outputs. Across all cases, standard accuracy metrics remain largely unchanged, confirming that calibration integrity is a distinct and consequential attack surface. Our core contributions are as follows:

Calibration integrity as a new attack surface: We identify predictive confidence calibration as a standalone attack objective in FL and demonstrate that it can be manipulated without

triggering accuracy-centric alarms.

Attack design and theoretical foundation: We propose the $\eta\text{-}\tau$ coupling mechanism and develop a non-convex convergence analysis under non-IID conditions, providing a theoretical foundation for why effective-step-size coupling preserves benign-like optimization behavior while enabling systematic confidence manipulation.

Stealthiness analysis: We empirically show that TSA produces benign-like training dynamics and update geometry that challenge similarity-based detectors and robust aggregators, maintaining high cosine similarity and representation alignment with benign updates.

Extensive evaluation and case studies: We validate TSA across various benchmarks and FL settings, demonstrate robustness against existing defenses, and demonstrate real-world implications through case studies in healthcare, autonomous driving, and language generation pipelines.

2 Background and Related Work

2.1 Security Threats in Federated Learning

The primary security surface in federated learning (FL) arises from malicious clients that can submit adversarial updates to the server during the collaborative training process. We note that we focus on client-side threats and do not consider server-side data inference attacks. Prior work has studied several families of attacks across diverse FL settings.

(i) *Untargeted model poisoning*. Adversaries perturb local updates to degrade global accuracy or slow convergence, using techniques such as sign flipping, scaled gradients, or noise injection [4, 29]. These attacks aim to disrupt the learning process and render the global model unusable. (ii) *Backdoor and targeted poisoning*. Attackers train on poisoned data so that inputs containing specific triggers are mapped to attacker-chosen labels while maintaining accuracy on clean data [3, 30, 48]. Model replacement attacks amplify this by scaling malicious updates to dominate the aggregation, effectively overwriting the global model with a backdoored version.

Byzantine-robust defenses and evasion. To counter malicious updates, robust aggregation mechanisms have been proposed, including Trimmed Mean [49], Krum [5], FLAME [39], and FLTrust [6]. In response, sophisticated adversaries have developed collusion strategies to evade these defenses by carefully shaping their updates to appear benign during the aggregation process [11].

Collectively, these lines of work optimize for correctness degradation or backdoors. While effective at causing visible failures, such attacks are often detected through accuracy-based monitoring or abnormal training dynamics. Moreover, the integrity of model *confidence* has received little attention despite its critical role in operational decisions, such as selective prediction, escalation logic, and human-in-the-loop review. Our work positions confidence calibration as an or-

thogonal threat dimension that can evade accuracy-centric monitors and standard robust aggregation while causing harm in confidence-dependent systems.

2.2 Model Confidence and Calibration

Most modern neural networks produce confidence estimates by converting real-valued scores into probabilities via the softmax function. Given an input sample x , a classifier outputs a logit vector $z(x) \in \mathbb{R}^C$ over C classes, and the predicted class distribution is

$$p_\theta(y = c | x) = \frac{\exp(z_c(x))}{\sum_{k=1}^C \exp(z_k(x))}, \quad c \in \{1, \dots, C\}. \quad (1)$$

The predicted label is $\hat{y}(x) = \arg \max_c p_\theta(y = c | x)$, and the associated confidence is $\hat{p}(x) = \max_c p_\theta(y = c | x)$. These probabilities are often treated as measures of model certainty and frequently drive downstream system behavior beyond evaluation purposes.

Confidence in operational systems. In safety-critical deployments, confidence is directly consumed by operational logic. For instance, in remote patient monitoring, on-device models escalate only low-confidence predictions to clinicians, avoiding continuous data upload. In autonomous driving, perception confidence gates conservative fallback behaviors. System correctness and resource allocation thus depend critically on whether predicted probabilities faithfully reflect empirical correctness, a property known as *calibration*.

Calibration metrics. The reliability of predicted probabilities is quantified using calibration metrics. Let $\{(x_i, y_i)\}_{i=1}^n$ be an evaluation set, and define $\hat{y}_i = \arg \max_c p_\theta(y = c | x_i)$, $\hat{p}_i = \max_c p_\theta(y = c | x_i)$, and $a_i = \mathbb{1}[\hat{y}_i = y_i]$ (correctness indicator). Expected Calibration Error (ECE) measures the discrepancy between confidence and accuracy by partitioning samples into M bins $\{B_m\}_{m=1}^M$ according to \hat{p}_i :

$$\text{ECE} = \sum_{m=1}^M \frac{|B_m|}{n} |\text{acc}(B_m) - \text{conf}(B_m)|, \quad (2)$$

where $\text{acc}(B_m) = \frac{1}{|B_m|} \sum_{i \in B_m} a_i$ and $\text{conf}(B_m) = \frac{1}{|B_m|} \sum_{i \in B_m} \hat{p}_i$ denote per-bin empirical accuracy and average confidence, respectively [17]. While ECE measures the magnitude of miscalibration, it discards directionality. This distinction matters: overconfidence suppresses escalation despite incorrect predictions, while underconfidence triggers unnecessary verification. Signed-ECE (sECE) retains this direction [24]:

$$\text{sECE} = \sum_{m=1}^M \frac{|B_m|}{n} (\text{acc}(B_m) - \text{conf}(B_m)), \quad (3)$$

where $\text{sECE} < 0$ indicates overconfidence and $\text{sECE} > 0$ indicates underconfidence. To build intuition, consider weather forecasting: when a service reports “30% chance of rain,” calibration requires that it actually rains on roughly 30% of

such forecasts. ECE quantifies the average deviation from this ideal, while sECE reveals whether the model systematically over- or under-predicts its correctness likelihood.

Complementary proper scoring rules evaluate probabilistic predictions without binning. Negative Log-Likelihood (NLL) is defined as

$$\text{NLL} = -\frac{1}{n} \sum_{i=1}^n \log p_\theta(y = y_i | x_i), \quad (4)$$

which heavily penalizes confident mistakes. The Brier score measures the squared error between the predicted distribution and the one-hot label $e(y_i) \in \{0, 1\}^C$:

$$\text{Brier} = \frac{1}{n} \sum_{i=1}^n \sum_{c=1}^C (p_\theta(y = c | x_i) - e(y_i)_c)^2. \quad (5)$$

In this work, we utilize ECE and sECE as primary metrics given their interpretable, deployment-oriented view of probability quality and their ability to distinguish between overconfidence and underconfidence, a distinction critical for understanding how calibration manipulation affects safety-critical decision logic.

2.3 Attacking Confidence Calibration

Prior work on attacking model calibration has largely focused on *inference-time* adversarial examples that craft input perturbations to induce miscalibration or unreliable uncertainty estimates [13, 27, 41]. These attacks typically modify inputs to alter the posterior distribution (e.g., confidence or entropy) without changing the predicted label, often requiring white-box access to model internals (architecture, parameters, logits) or repeated black-box queries [8, 16, 35]. While effective in controlled settings, such approaches face two fundamental challenges in real-world deployments.

First, they assume the attacker can compute or estimate sensitive model signals, which may be unavailable due to API restrictions, output rounding, rate limits, or privacy constraints. Second, even when perturbations can be generated, their effectiveness degrades substantially in physical deployments due to sensing noise, compression artifacts, domain shifts, and non-differentiable pre-processing [10, 18, 26, 31, 32]. These challenges are amplified in federated learning, where adversaries cannot control other clients’ inputs or consistently access the global model’s gradients at inference across devices. Consequently, inference-time calibration attacks do not naturally extend to FL threat models that operate through local training.

In contrast, *training-time* manipulation of model confidence has received limited attention. Most FL attacks focus on degrading accuracy, targeted misclassification, or implanting backdoors [3, 11, 34], objectives orthogonal to calibration integrity that can often be detected via accuracy monitoring or misprediction patterns. Our work addresses this gap by

treating calibration as a first-class attack objective in FL. We propose a training-time mechanism that systematically biases the model’s confidence through temperature-controlled local optimization, without requiring inference-time perturbations or access to other clients’ data.

2.4 Temperature Scaling

Most modern neural networks include an explicit normalization step that converts real-valued outputs into a probability distribution. In particular, for classification, a model produces a logit vector $z(x) \in \mathbb{R}^C$ for an input x , and the categorical predictive distribution is obtained via the softmax function (Eq. 1). This distribution is commonly paired with the cross-entropy loss, which enables end-to-end training by comparing the predicted probabilities to the ground-truth label.

Temperature scaling is a simple yet widely used mechanism for controlling the sharpness of the softmax distribution by rescaling logits with a positive scalar $\tau > 0$,

$$p_{\theta}^{(\tau)}(y=c \mid x) = \frac{\exp(z_c(x)/\tau)}{\sum_{j=1}^C \exp(z_j(x)/\tau)}. \quad (6)$$

Larger temperatures ($\tau > 1$) produce smoother, less peaked distributions, while smaller temperatures ($\tau < 1$) sharpen the distribution. It is important to note that throughout this work, we implicitly assume $\tau > 0$, we use $\tau < 1$ to denote $0 < \tau < 1$.

While temperature has been most commonly used as an inference-time control knob in cases such as knowledge distillation [19], post-hoc calibration [17] or probabilistic sampling [22, 52, 54], recent work has begun to study temperature as a training-time factor that can meaningfully alter learning dynamics. In particular, Agarwala et. al analyze how softmax temperature interacts with optimization and generalization under softmax-cross-entropy training, highlighting that temperature can effectively modulate the training behavior beyond merely reshaping probabilities at test time [1].

In parallel, emerging work has explored temperature scaling during federated local training to improve convergence and generalization [33]. Our work extends this theoretical foundation from convex, IID settings to realistic non-convex, non-IID federated environments. Crucially, we identify the learning rate–temperature coupling as fundamental: maintaining a constant effective step size $\beta = \eta/\tau$ preserves benign-style convergence bounds under client drift while enabling systematic confidence distortion. This finding serves an adversarial purpose (i.e., evading detection while degrading calibration) rather than improving performance.

3 Threat Model

Goals and Capability. We define the adversary’s goal as manipulating the model confidence calibration toward either under- or over-confidence states, while keeping predictive

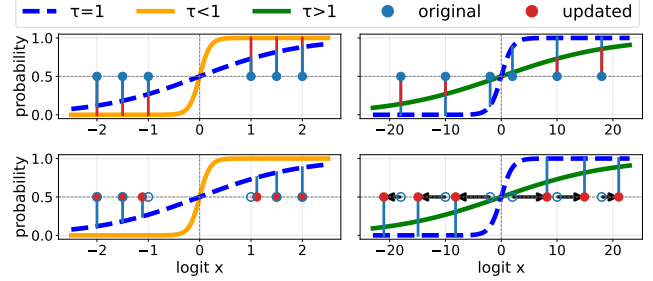


Figure 1: Effect of training-time temperature scaling on logit updates and test-time confidence. Solid curves show the τ -scaled sigmoid used to compute updates (—: $\tau < 1$, —: $\tau > 1$), while evaluation uses the standard $\tau=1$ mapping (---), so updated logits (● → ●) can yield shifted probabilities and degraded calibration; note the different x-axis ranges.

accuracy ostensibly unchanged. Regarding capability, we assume the adversary has full control over the local training process on its own compromised devices, including access to local data, model parameters, and the ability to modify the training procedure. Concretely, the attacker can choose the training temperature τ and adjust the local learning rate (η) accordingly during standard local optimization. We note that these capabilities are standard in the FL security literature.

Assumptions. We assume that attackers can control local training but cannot interfere with server-side aggregation or benign clients, and that the fraction of malicious participants is less than 50% [11]. The adversary can not manipulate other clients’ training process or data, and has no control over any computation performed at the server.

4 Temperature Scaling Attack

In this section, we present the design of the proposed *temperature scaling attack*. We begin by developing an analytic rationale for temperature scaling from a decision-boundary perspective, clarifying how it can substantially reshape predictive confidence while largely preserving the underlying decision regions. Building on this interpretation, we describe the attack mechanism, which injects carefully regulated temperature scaling into local training to steer confidence and calibration with minimal impact on accuracy. Finally, we provide a convergence-based analysis that explains why the resulting model updates can remain difficult to distinguish from benign updates while still inducing systematic miscalibration.

4.1 Rationale

Figure 1 illustrates the core mechanism of TSA in a simplified binary classification setting with a sigmoid (i.e., binary softmax) output $\sigma(x) = \frac{1}{1+e^{-x}}$. Under standard training and evaluation, a logit z is mapped to a probability $p = \sigma(z)$. TSA

perturbs this pipeline only during training by applying temperature scaling to the probability mapping, $p_\tau = \sigma(\frac{z}{\tau})$, thereby altering the geometric correspondence between logits and probabilities—and thus the gradient signal driving optimization—while evaluation still uses the unscaled mapping $\sigma(z)$ (i.e., $\tau = 1$).

The top row visualizes this mismatch at the level of mappings. When $\tau < 1$ (left column), the sigmoid becomes steeper and saturates earlier: logits that would be moderately confident under $\tau = 1$ can already be interpreted as high-confidence under $\sigma(z/\tau)$. Conversely, when $\tau > 1$ (right column), the sigmoid flattens and expands the effective probability range: the same logits are mapped to less extreme probabilities, making predictions appear less confident in the τ -scaled training space. Consequently, identical logits correspond to systematically different confidence values depending on τ , even before any parameter update is applied.

The bottom row shows how this distortion induces biased logit updates via a single gradient step. For $\tau < 1$, samples that are underconfident under the evaluation mapping $\sigma(z)$ may already fall into a saturated, high-confidence regime under $\sigma(z/\tau)$, where gradients are strongly attenuated; their logits therefore move little, yielding underconfident outputs at test time in the logit space. In contrast, for $\tau > 1$, samples that are already overconfident under $\sigma(z)$ can be mapped to an underconfident regime under $\sigma(z/\tau)$, keeping gradients “alive” and pushing logits further, which translates into even more overconfident predictions when evaluated with $\tau = 1$. In summary, training-time temperature scaling effectively trains the model in a distorted logit–probability space but deploys it in the original space, forcing logits toward under/over-confident regimes and inducing intended miscalibration.

However, naively applying temperature scaling during local training can induce convergence instability or degrade accuracy, since it directly reshapes the gradients that drive optimization. To address this, Section 4.3 provides a theoretical convergence analysis showing that TSA can preserve stable convergence under this perturbation.

4.2 Overall Workflow

We present the overall workflow of the temperature scaling attack in a standard federated learning setting. First, the server broadcasts the current global model to participating clients and each client then performs local training on its own data. Here, malicious clients additionally configure the local learning rate η and the training softmax temperature τ to steer the global model toward overconfidence ($\tau > 1$) or underconfidence ($\tau < 1$). In particular, when an attacker configures the training temperature τ , it scales the local learning rate to $\eta \cdot \tau$. We note that this learning rate–temperature (η – τ) coupling is carefully chosen based on our theoretical convergence analysis (c.f., Sec. 4.3). After local training, all clients, including attackers, take a typical federated learning operation and up-

load their model updates (e.g., parameters or gradients) to the server. Finally, the server aggregates the received updates using its aggregation rule to produce an updated global model.

4.3 Theoretical Convergence Analysis

Now we analyze temperature-scaled local training in the standard non-convex FL convergence framework and formalize a key invariance: if each client k maintains a common *effective step size* $\beta \triangleq \eta_k/\tau_k$, where η_k and τ_k denote the local learning rate and temperature, then its local optimization dynamics admit the same type of convergence bound as benign training, up to controlled drift and stochastic noise terms. Concretely, we consider K clients collaboratively minimizing $F(\theta) \triangleq \sum_{k=1}^K p_k f_k(\theta)$, where w denotes the model parameters, p_k is the aggregation weight (e.g., proportional to the local data size), and $f_k(\theta) = \mathbb{E}_{\xi \sim \mathcal{D}_k} [\ell(\theta; \xi)]$ is a non-convex local objective. Here, ξ denotes a random training sample drawn from client k ’s data distribution \mathcal{D}_k . In each communication round t , client k starts from the global model θ_t and performs E local SGD steps with (η_k, τ_k) using the temperature-scaled loss ℓ_{τ_k} that applies softmax(\cdot/τ_k).

Now we outline the assumptions we consider for the convergence analysis.

Assumption 1 (Smoothness of base objective). *For each client k , f_k is L -smooth with a Lipschitz constant L :*

$$\|\nabla f_k(u) - \nabla f_k(v)\| \leq L\|u - v\|, \quad \forall u, v. \quad (7)$$

Assumption 2 (Unbiased and bounded stochastic gradients). *Let $\mathbf{g}_k(\theta; \xi)$ be a stochastic gradient on client k . Then*

$$\mathbb{E}_{\xi}[\mathbf{g}_k(\theta; \xi)] = \nabla f_k(\theta) \quad \text{and} \quad (8)$$

$$\mathbb{E}_{\xi}[\|\mathbf{g}_k(\theta; \xi) - \nabla f_k(\theta)\|^2] \leq \sigma^2, \quad \forall \theta. \quad (9)$$

Assumption 3 (Bounded heterogeneity). *There exists Γ^2 such that, for all θ ,*

$$\sum_{k=1}^K p_k \|\nabla f_k(\theta) - \nabla F(\theta)\|^2 \leq \Gamma^2. \quad (10)$$

Assumption 4 (Constant effective step size). *Clients may use different learning rates η_k and temperatures τ_k , but satisfy:*

$$\eta_k/\tau_k = \beta, \quad \forall k \in [K]. \quad (11)$$

Temperature-dependent curvature and stability. For softmax cross-entropy, temperature rescales curvature. Therefore, increasing τ smooths the predictive distribution and reduces the effective curvature of the loss.

Lemma 1 (Temperature-dependent smoothness). *Consider the temperature-scaled softmax cross-entropy loss $\ell_{\tau}(\theta; x, y)$. Assume the logit vector $\mathbf{z}(\theta; x) \in \mathbb{R}^K$ is twice differentiable*

and its Jacobian w.r.t. Θ is bounded as $\|\mathbf{J}_\Theta \mathbf{z}(\Theta; x)\| \leq G(x)$, where $G(x)$ is an input-dependent upper bound on the sensitivity of logits to parameter perturbations (i.e., a Lipschitz-type bound of \mathbf{z} in Θ at input x). Then the Hessian satisfies

$$\|\nabla_\Theta^2 \ell_\tau(\Theta; x, y)\| \leq \frac{C(x)}{\tau^2}, \quad (12)$$

for some $C(x)$ depending on $G(x)$ and $\|x\|$. Consequently, the population objective is L -smooth with $L_{T=\tau} \leq \bar{C}/\tau^2$ for $\bar{C} \triangleq \mathbb{E}[C(x)]$.

Lemma 1 implies that the temperature-scaled objective admits a smaller Lipschitz smoothness constant, scaling as $L_{T=\tau} = O(1/\tau^2)$ up to problem-dependent constants. As a result, even with clients utilizing heterogeneous (η_k, τ_k) , enforcing (11) aligns their effective step size $\beta = \eta_k/\tau_k$ and maintains the local update scale comparable across clients. This yields optimization dynamics that satisfy the same type of step-size stability conditions as benign training (up to controlled constants), while allowing the attacker to steer calibration through τ . In addition, combining $\eta_k = \beta\tau_k$ with the τ -induced rescaling of the gradient (Lemma 1) yields the cancellation $\eta_k \nabla \ell_{\tau_k} \approx \beta \nabla \ell_1$, which explains why the convergence trajectory can remain benign-looking under the attack.

Under the aforementioned assumptions and Lemma 1, the standard descent analysis yields an upper bound on the average squared gradient norm of the global objective:

Theorem 1 (Non-convex convergence with constant β).

$$\frac{1}{T} \sum_{t=0}^{T-1} \mathbb{E}[\|\nabla F(\Theta_t)\|^2] \leq \frac{2(F(\Theta_0) - F^*)}{\beta ET} + \underbrace{\frac{\beta L \sigma^2}{M}}_{\text{variance}} + \underbrace{\beta^2 L^2 E^2 \Gamma^2}_{\text{client drift}}, \quad (13)$$

where T is the number of communication rounds, M is the number of participating clients per round, and F^* denotes $\inf_\Theta F(\Theta)$. Eq. (13) matches the canonical non-convex FL convergence form: the first term vanishes as T grows, the second decreases with more participants, and the third captures a non-IID error floor controlled by β and E . Importantly, because $\beta = \eta/\tau$ is a tunable hyperparameter (like η), an attacker can adjust (η, τ) jointly to keep β aligned with benign optimization and therefore retain a benign-like convergence profile at the level of model updates, while still reshaping predictive confidence through temperature.

5 Evaluation

5.1 Setup

We now present extensive experimental results using three benchmarks, including comparisons against diverse baselines and a set of case studies. We detail the evaluation setup below.

TEMP.	ACCURACY (%)	ECE (%)	sECE (%)	BRIERSCORE	NLL
1	91.57 \pm 0.23	3.11 \pm 0.35	3.06 \pm 0.35	0.13 \pm 0.00	0.29 \pm 0.00
2	91.46 \pm 0.31	0.85 \pm 0.40	-0.56 \pm 0.63	0.13 \pm 0.00	0.29 \pm 0.01
3	91.33 \pm 0.33	2.78 \pm 0.68	-2.74 \pm 0.68	0.13 \pm 0.01	0.32 \pm 0.02
4	91.19 \pm 0.40	4.11 \pm 0.72	-4.11 \pm 0.72	0.14 \pm 0.01	0.37 \pm 0.03
5	91.09 \pm 0.45	5.02 \pm 0.72	-5.01 \pm 0.73	0.14 \pm 0.01	0.43 \pm 0.04
0.5	91.46 \pm 0.26	4.76 \pm 0.34	4.75 \pm 0.33	0.13 \pm 0.00	0.30 \pm 0.01
0.33	91.43 \pm 0.24	5.11 \pm 0.36	5.10 \pm 0.36	0.13 \pm 0.00	0.30 \pm 0.01
0.25	91.41 \pm 0.23	5.23 \pm 0.38	5.22 \pm 0.38	0.13 \pm 0.00	0.30 \pm 0.01
0.2	91.40 \pm 0.25	5.29 \pm 0.39	5.28 \pm 0.38	0.14 \pm 0.00	0.31 \pm 0.01

Table 1: Global model accuracy and confidence metrics with varying temperature on MNIST-MLP configuration.

Dataset and Models. For the overall evaluation, we consider three dataset-model configuration pairs that cover increasing task difficulty and model capacity:

- **MNIST-MLP:** The MNIST handwritten digits are paired with a lightweight multi-layer perceptron (MLP), serving as a simple sanity-check benchmark for analyzing confidence manipulation under a controlled setting.
- **CIFAR10-CNN:** For CIFAR-10 we use a standard convolutional neural network (CNN) to evaluate the attack on natural images, where calibration is known to be challenging.
- **CIFAR100-ResNet18:** The CIFAR-100 data set is configured with ResNet-18 to study the attack under a larger label space and a stronger backbone, which typically amplifies calibration errors and stresses robustness to heterogeneity.

Federated Learning Configuration. Unless otherwise specified, we adopt a standard synchronous FL setup using FedAvg. In each FL round, the server samples 5 clients (10%) uniformly at random from a total of 50 clients and broadcasts the current global model. Each selected client performs 5 steps of local SGD on its private data and returns either model parameters or model updates to the server, which aggregates them using data-size weights p_k . To reflect realistic statistical heterogeneity, we construct non-IID client partitions using a Dirichlet split [21] with concentration parameter $\alpha=1.0$ (smaller α indicates higher heterogeneity), otherwise specified. We report results averaged over 5 independently selected random seeds and evaluate both predictive performance and calibration using accuracy and calibration metrics.

5.2 Overall Attack Performance

MNIST-MLP. On MNIST-MLP, accuracy stays nearly constant (around 91%) across all τ , but calibration shifts in a predictable direction. For $\tau > 1$, sECE becomes increasingly negative, indicating growing *over-confidence*; for $\tau < 1$, sECE becomes strongly positive, indicating *under-confidence*, with ECE generally increasing as $|\tau - 1|$ grows. While ECE is numerically smaller at $\tau=2, 3$ than at $\tau=1$, this mainly reflects a *trend shift* from a slightly under-confident benign model (positive sECE) toward over-confidence (negative sECE), not a guaranteed improvement in reliability. At larger temperatures, calibration degrades in both signed and unsigned terms (e.g.,

TEMP.	ACCURACY (%)	ECE (%)	SECE (%)	BRIERSCORE	NLL
1	68.55 \pm 0.73	1.56 \pm 0.59	-0.84 \pm 1.05	0.43 \pm 0.01	0.89 \pm 0.02
2	68.63 \pm 0.86	6.01 \pm 0.36	-6.00 \pm 0.35	0.43 \pm 0.01	0.92 \pm 0.02
3	68.46 \pm 0.61	9.08 \pm 1.31	-9.08 \pm 1.31	0.44 \pm 0.00	0.98 \pm 0.04
4	68.04 \pm 0.47	11.66 \pm 2.57	-11.64 \pm 2.59	0.46 \pm 0.02	1.05 \pm 0.09
5	67.63 \pm 0.79	13.46 \pm 3.11	-13.43 \pm 3.13	0.47 \pm 0.03	1.12 \pm 0.15
0.5	68.61 \pm 0.77	3.89 \pm 2.61	3.81 \pm 2.67	0.43 \pm 0.00	0.90 \pm 0.01
0.33	68.46 \pm 0.72	5.96 \pm 3.12	5.89 \pm 3.14	0.43 \pm 0.00	0.91 \pm 0.01
0.25	68.40 \pm 0.76	6.68 \pm 3.38	6.64 \pm 3.40	0.44 \pm 0.00	0.92 \pm 0.01
0.2	68.27 \pm 0.68	7.72 \pm 4.27	7.72 \pm 4.26	0.44 \pm 0.00	0.93 \pm 0.01

Table 2: Global model accuracy and confidence metrics with varying temperature on CIFAR10-CNN configuration.

TEMP.	ACCURACY (%)	ECE (%)	SECE (%)	BRIERSCORE	NLL
1	36.24 \pm 0.76	15.59 \pm 0.77	-15.59 \pm 0.77	0.80 \pm 0.01	2.71 \pm 0.03
2	37.20 \pm 0.84	24.22 \pm 1.33	-24.22 \pm 1.33	0.84 \pm 0.02	2.93 \pm 0.08
3	37.78 \pm 0.61	30.24 \pm 2.28	-30.24 \pm 2.28	0.88 \pm 0.02	3.26 \pm 0.15
4	37.47 \pm 0.71	35.39 \pm 3.84	-35.39 \pm 3.84	0.93 \pm 0.03	3.74 \pm 0.38
5	37.57 \pm 0.56	38.19 \pm 5.47	-38.18 \pm 5.47	0.95 \pm 0.05	4.15 \pm 0.64
0.5	35.74 \pm 0.67	10.41 \pm 2.84	-10.41 \pm 2.84	0.79 \pm 0.01	2.64 \pm 0.08
0.33	35.03 \pm 0.65	9.31 \pm 3.26	-9.30 \pm 3.27	0.79 \pm 0.01	2.64 \pm 0.06
0.25	35.63 \pm 0.72	7.93 \pm 3.80	-7.93 \pm 3.80	0.79 \pm 0.01	2.61 \pm 0.06
0.2	35.41 \pm 0.43	11.62 \pm 6.02	-2.93 \pm 13.94	0.80 \pm 0.04	2.69 \pm 0.14

Table 3: Global model accuracy and confidence metrics with varying temperature on CIFAR100-ResNet18 configuration.

up to $ECE = 5.02$ and $sECE = -5.01$ at $\tau=5$), and proper scoring rules (Brier/NLL) also worsen.

CIFAR10-CNN. A similar but amplified pattern holds on CIFAR10-CNN (Table 2). Accuracy remains tightly clustered around 68%, yet calibration deteriorates sharply as τ moves away from 1. For $\tau > 1$, the model becomes progressively *over-confident*: ECE rises from 1.56 ($\tau=1$) to 6.01, 9.08, 11.66, and 13.46 for $\tau=2-5$, with sECE tracking the same direction (-6.00 to -13.43). For $\tau < 1$, the trend flips to *under-confidence*: ECE increases to 3.89–7.72 for $\tau=0.5-0.2$ and sECE becomes positive with comparable magnitudes (3.81–7.72). Brier and NLL also increase as confidence distortion strengthens (e.g., NLL $0.89 \rightarrow 1.12$ and Brier $0.43 \rightarrow 0.47$ from $\tau=1$ to $\tau=5$), confirming that probability quality worsens even when accuracy is preserved.

CIFAR100-ResNet18. CIFAR100-ResNet18 is already severely miscalibrated and *over-confident* at $\tau=1$ (ECE/sECE = 15.59/–15.59). Raising τ worsens calibration dramatically while accuracy stays in the mid-30% range: ECE increases to 24.22, 30.24, 35.39, and 38.19 for $\tau=2-5$ (with sECE matching), and Brier/NLL deteriorate accordingly (Brier $0.80 \rightarrow 0.95$, NLL $2.71 \rightarrow 4.15$ at $\tau=5$). Lowering τ can reduce ECE in some cases (e.g., 10.41 at $\tau=0.5$, 7.93 at $\tau=0.25$), but the behavior is less monotonic and becomes unstable at very low τ (e.g., $\tau=0.2$). Overall, across all three benchmarks, temperature scaling enables large, directional calibration shifts with only minor accuracy changes.

Calibration drift under temperature scaling. Figure 2 visualizes how training-time temperature scaling systematically distorts the global model’s confidence behavior on CIFAR10–

CNN. When $\tau < 1$, the confidence mass shifts toward smaller values and the reliability curve lies above the diagonal, indicating under-confidence where empirical accuracies exceed predicted confidences across bins. When $\tau > 1$, confidences concentrate near one, and the reliability curve falls below the diagonal, revealing a pronounced over-confidence gap where predicted confidences consistently exceed empirical accuracies. Notably, these calibration shifts occur while accuracy remains largely stable, confirming that temperature scaling provides a direct control knob for steering the *direction* of miscalibration without requiring large changes in accuracy.

5.3 Benign-Aligned Updates

In this section, we show that temperature scaling produces updates that are difficult to distinguish from benign behavior, and further demonstrate that the proposed learning rate–temperature coupling (via the effective step size β) is essential for maintaining such benign-like updates. We examine detectability from three complementary perspectives: (i) the convergence trajectory in terms of round-wise global accuracy, (ii) the update geometry in parameter space via gradient analysis, and (iii) the similarity of learned representations.

Convergence Trajectory. A straightforward server-side defense is to monitor the convergence trajectory using a held-out validation set, e.g., by tracking round-wise accuracy or loss. Figure 3 plots the global test accuracy (left) and sECE (right) over communication rounds on CIFAR10-CNN. As shown, the accuracy trajectories under different training temperatures almost completely overlap, with no statistically meaningful separation, indicating that accuracy-only monitoring is insufficient to reveal the presence of the attack. In contrast, sECE shifts systematically with temperature: for $\tau > 1$, sECE becomes more negative than the benign setting ($\tau=1$), reflecting increased over-confidence, whereas for $\tau < 1$, sECE moves to positive values, indicating under-confidence. These results suggest that observing standard convergence metrics alone is unlikely to detect temperature scaling attacks, even though the attack induces pronounced and directional calibration drift.

Parameter Space Analysis. Beyond simple trajectory monitoring, many existing defenses in federated learning analyze client-submitted parameters or gradients, leveraging the intuition that malicious clients will produce *atypical* updates in parameter space. To evaluate temperature scaling attack under such update-space scrutiny, we measure update-direction similarity after 10 local SGD steps on CIFAR10-CNN. Specifically, we define the local update as the parameter displacement $\Delta\theta \triangleq \theta_{\text{after}} - \theta_{\text{before}}$ and compute the cosine similarity $\cos(\Delta\theta_{\tau=1}, \Delta\theta_{\text{attack}})$, where $\Delta\theta_{\tau=1}$ is the benign update obtained with $\tau=1$ and $\Delta\theta_{\text{attack}}$ is the update produced under a given attack condition. To contextualize the results, we compare against two conventional poisoning baselines: noise injection and label flipping. For noise injection, we perturb the update as $\Delta\theta \leftarrow \Delta\theta + \epsilon$ with $\epsilon \sim \mathcal{N}(0, \sigma^2)$ and

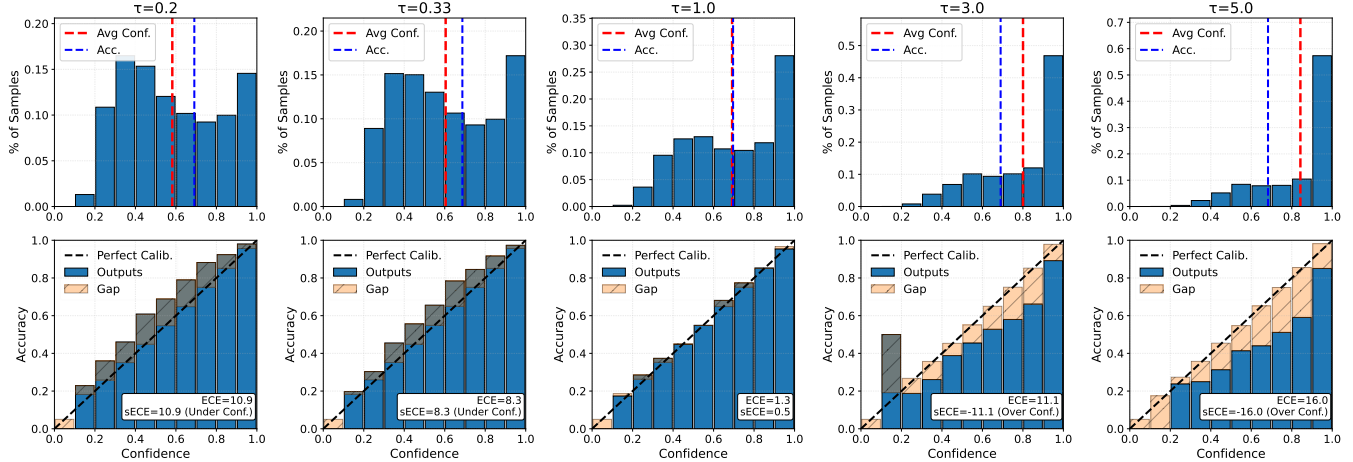


Figure 2: Confidence distribution and reliability diagrams under different training temperatures τ on CIFAR10–CNN.

Top row: histogram of predicted confidences with **average confidence** (red dashed) and **accuracy** (blue dashed).

Bottom row: reliability diagrams showing the gap between bin accuracy and confidence. Low temperatures ($\tau < 1$) induce under-confidence, while high temperatures ($\tau > 1$) induce over-confidence, despite accuracy remaining largely unchanged.

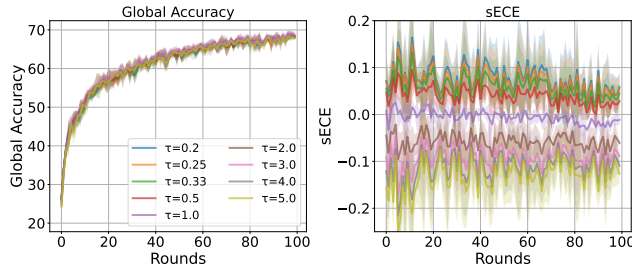


Figure 3: Global accuracy (left) and sECE (right) over rounds on CIFAR10–CNN for different training temperatures τ . Accuracy remains similar across τ , while sECE shifts systematically, indicating controllable under-/over-confidence.

$\sigma \in \{10^{-1}, 5 \times 10^{-2}, 1 \times 10^{-2}\}$. For label flipping, we shift labels by k with modulo over C classes, $y \leftarrow (y + k) \bmod C$, using $k \in \{1, 2, 3, 4, 5\}$ (larger shifts are redundant by symmetry). Figure 4 visualizes the cosine similarity between benign updates and the updates produced by each attack.

As shown in Figure 4, conventional poisoning attacks substantially reduce cosine similarity, typically around 0.2 or lower, indicating that their updates deviate markedly from benign optimization directions. In contrast, temperature scaling preserves near-collinearity with benign updates across a wide range of temperatures, with the minimum similarity still around 0.93. This suggests that temperature scaling attacks can remain difficult to flag using parameter space analysis, even while inducing systematic and directional confidence manipulation.

Representation Space Analysis. We next study whether representation-based monitoring, which is orthogonal to trajectory- and parameter-space checks, can distinguish tem-

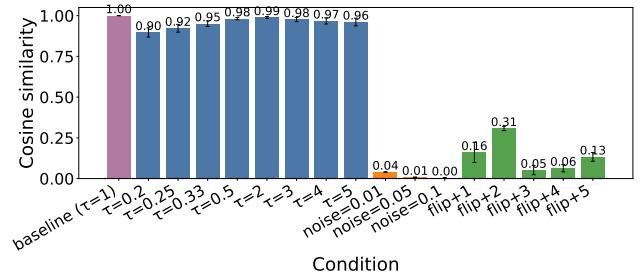


Figure 4: Cosine similarity between benign updates (baseline, $\tau=1$) and updates under different attacks. Temperature scaling maintains high similarity with benign gradients, whereas noise addition and label flipping sharply reduce similarity.

perature scaling attacks. We focus on two commonly used signals: (i) the penultimate-layer representation, which reflects the high-dimensional features learned by the network, and (ii) the classifier logits, which capture the model’s categorical response to an input. To compare penultimate representations, we use Centered Kernel Alignment (CKA), which is invariant to common symmetries such as orthogonal rotations and is thus better suited than cosine similarity for high-dimensional feature maps. For logits, we use cosine similarity. Figure 5 first establishes a benign reference by training the same CIFAR10–CNN configuration with five different random seeds (5 epochs) and computing pairwise similarities. Even without any attack, independent runs exhibit non-trivial variability, yet both logit cosine similarity and penultimate CKA typically remain above ~ 0.8 . We treat this range as a practical baseline for “benign” similarity.

Using this reference, Figure 6 compares attacked models

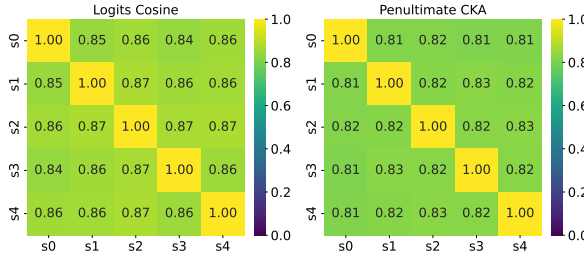


Figure 5: Seed-to-seed similarity under benign training ($\tau=1$): pairwise logit cosine similarity (left) and penultimate-layer CKA (right) on the same testset.

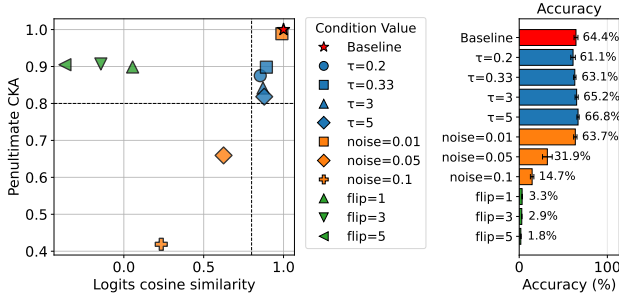


Figure 6: Logit cosine similarity vs. penultimate-layer CKA (left) and test accuracy (right) under different attack conditions, measured against the benign baseline.

against the benign baseline. Conventional poisoning baselines produce readily observable deviations. Noise injection exhibits a clear trade-off: the mild setting ($\sigma=0.01$) stays relatively close to the baseline in similarity but also fails to meaningfully impact accuracy, whereas larger noise levels ($\sigma=0.05, 0.1$) sharply reduce similarity and severely degrade accuracy. Label flipping shows a distinctive signature: penultimate CKA remains high while logit cosine similarity becomes very low, consistent with preserving feature extractors but permuting output semantics.

In contrast, temperature scaling remains largely within the benign similarity range while preserving utility. Across all tested temperatures, logit cosine similarity stays high (≥ 0.85) and penultimate CKA remains above ~ 0.8 , with accuracy comparable to (and sometimes slightly higher than) the baseline (e.g., 61.1–66.8% vs. 64.4%). Overall, these results suggest that temperature scaling can evade a broad class of representation-based detectors without incurring the accuracy degradation or pronounced representation drift that characterizes conventional poisoning baselines.

Role of η – τ coupling. Importantly, the benign-like behavior of the temperature scaling attack is not incidental. We attribute this property to the proposed effective step-size (β) control, i.e., the learning rate–temperature coupling that enforces a constant $\beta = \eta/\tau$. To isolate its impact, Figure 7 measures

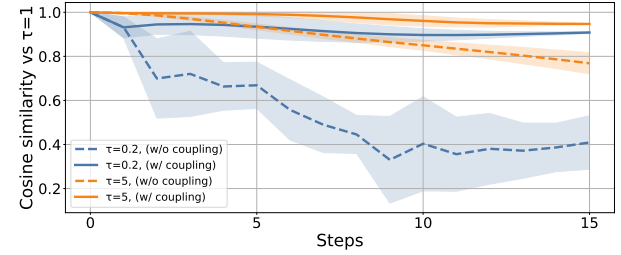


Figure 7: Cosine similarity to the $\tau=1$ update across local steps for $\tau=0.2$ and $\tau=5$, with and without η – τ coupling ($\beta = \eta/\tau$). Coupling preserves high similarity over steps, while removing it causes updates to diverge.

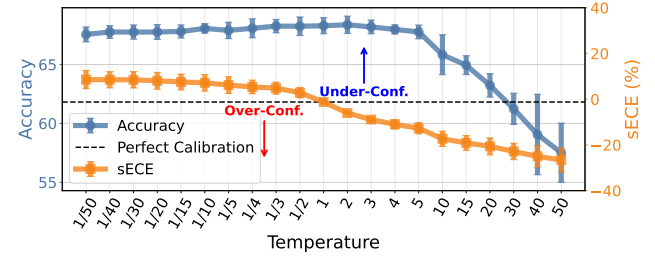


Figure 8: Effect of extreme temperatures under a fixed effective step size $\beta = \eta/\tau$ on CIFAR10–CNN. While sECE decreases monotonically as τ increases, overly large τ overly smooths the predictive distribution and weakens gradients, causing a noticeable accuracy drop beyond $\tau \approx 10$ and violating the accuracy-preservation of the attack.

the cosine similarity to the benign update across increasing numbers of local SGD steps, comparing temperature scaling with and without η – τ coupling for $\tau=0.2$ and $\tau=5$.

With coupling, updates remain highly aligned with the benign direction throughout local training in both cases. In contrast, without coupling, changing τ directly perturbs the optimization dynamics, and the update direction drifts away from the benign trajectory as local steps accumulate. We observe a more dramatic drop for $\tau=0.2$ than for $\tau=5$, which is consistent with prior findings that $\tau < 1$ can induce more aggressive training dynamics than $\tau > 1$ during optimization [33]. Overall, these results confirm that η – τ coupling is crucial for preserving benign-like update geometry, thereby enabling calibration manipulation while keeping the attack difficult to flag.

How far can τ be pushed under a fixed β ? The preceding analysis shows that enforcing a constant effective step size $\beta = \eta/\tau$ is critical for producing benign-like updates. A natural question is whether the attacker can choose arbitrarily small or large temperatures as long as the η – τ coupling is satisfied. Figure 8 sweeps τ while keeping β fixed and tracks both global accuracy and sECE. As τ increases, sECE decreases monotonically, showing that the attacker can con-

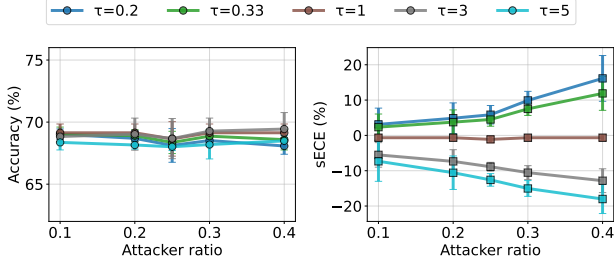


Figure 9: Effect of attacker ratio on global accuracy (left) and sECE (right) under different training temperatures τ .

tinuously steer the model toward over-confidence. However, beyond a moderate range, overly large τ noticeably degrades accuracy (starting around $\tau \approx 10$), violating the attack goal of preserving predictive performance.

This breakdown is consistent with a *signal erasure* interpretation. While fixing β maintains update *stability*, high temperature excessively smooths $\mathbf{p}_\tau = \text{softmax}(\mathbf{z}/\tau)$ toward a near-uniform distribution, collapsing logit margins and weakening class-discriminative gradient signals. Moreover, Lemma 1 implies $L_\tau = O(1/\tau^2)$, so the landscape becomes overly flat, and the signal-to-noise ratio deteriorates as useful gradients fade faster than stochastic noise. At the other extreme, very small τ can induce more aggressive and potentially unstable optimization dynamics, as also suggested by the divergence trends without coupling in Figure 7. Overall, η – τ -coupling is *necessary but not sufficient*: achieving a favorable impact–stealth trade-off requires choosing τ within a moderate range.

5.4 Robustness and Sensitivity Analysis

We now conduct a sensitivity analysis over three key factors that jointly govern the effectiveness and practicality of the proposed temperature scaling attack in federated learning: (i) the attacker ratio, (ii) the degree of non-IID data heterogeneity, and (iii) the effective step size β (i.e., η – τ coupling).

Resilience to Malicious Participation (Attacker ratio). Figure 9 reports how the global model’s test accuracy (left) and signed ECE (right) change as we vary the attacker ratio in the client population. Across all temperatures, accuracy stays nearly flat as the attacker ratio increases from 0.1 to 0.4, indicating that the attack remains hard to notice through standard utility monitoring. In contrast, calibration drift amplifies with more attackers. For high-temperature settings ($\tau > 1$), sECE becomes increasingly negative as the attacker ratio grows, reflecting stronger *over-confidence*; for low temperatures ($\tau < 1$), sECE becomes increasingly positive, reflecting stronger *under-confidence*. Notably, even with only 10% attackers, sECE already separates from the benign reference ($\tau=1$), and at 40% attackers the deviation reaches roughly ± 18 – 19 percentage points depending on the attack direction. Overall, this result shows that attack impact scales with

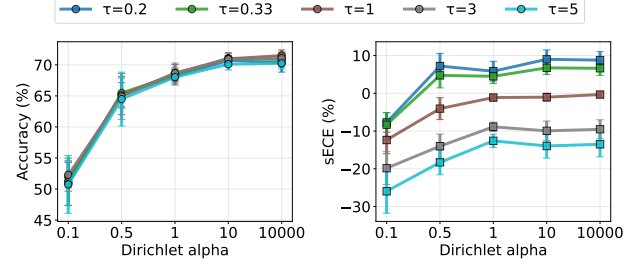


Figure 10: Effect of non-IID degree (Dirichlet α) on global accuracy and sECE under different training temperatures τ .

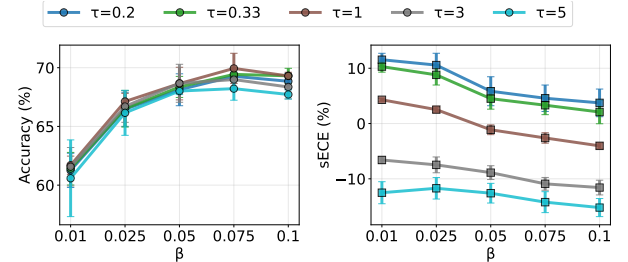


Figure 11: Sensitivity to the effective step size β under different training temperatures τ .

attacker participation while largely preserving accuracy, reinforcing that calibration is a more sensitive signal than performance for auditing this threat.

Robustness to Statistical Heterogeneity (Non-IID). Non-IID data distributions are the norm in practical federated learning, making it essential to evaluate whether temperature scaling remains effective under heterogeneous client data. Figure 10 varies the Dirichlet concentration parameter α to control the strength of non-IIDness and reports the resulting global accuracy and sECE. As expected, stronger heterogeneity (smaller α , e.g., $\alpha=0.1$) degrades overall utility, and the calibration baseline also shifts (sECE becomes more biased), reflecting the increased training difficulty under severe distribution skew. Crucially, however, the *relative* effect of temperature scaling remains consistent across α : for $\tau < 1$, sECE systematically increases (under-confidence), while for $\tau > 1$, sECE decreases (over-confidence), with accuracy trajectories remaining tightly clustered across temperatures within each α setting. This indicates that the attack is robust to realistic non-IID conditions, even as heterogeneity changes the absolute operating point, the attacker can still steer the *direction* of miscalibration in a controlled way without introducing conspicuous accuracy drops.

Invariance to Effective Step Size (β). Finally, Figure 11 studies how our key control knob (the effective step size $\beta = \eta/\tau$) affects both utility and calibration manipulation. Note that β coincides with the learning rate when $\tau=1$, so it naturally exhibits a task-dependent “sweet spot” for stable and accurate

training. Accordingly, varying β induces some deviation in both accuracy and sECE across all conditions. Nevertheless, the central takeaway remains unchanged: within a reasonable β range, temperature scaling preserves accuracy close to the benign reference ($\tau=1$) while still steering sECE in the intended direction. Specifically, $\tau < 1$ consistently increases sECE (under-confidence) and $\tau > 1$ decreases sECE (over-confidence), indicating that calibration control is robust to moderate changes in β even though β itself governs the overall optimization regime.

5.5 Evaluation against Existing Defenses

We now evaluate the proposed temperature scaling attack under representative defenses used in practice. We consider two broad axes: (i) *server-side robust aggregation* that aims to suppress malicious client updates during training, and (ii) *post-hoc calibration* that attempts to correct the confidence of the learned global model using a held-out validation set.

Byzantine-robust aggregation. Figure 12 reports the global accuracy and sECE achieved by four aggregation rules: FedAvg [36] (no defense), FLTrust [6], FoolsGold [12], and MultiKrum [5]. FedAvg serves as the baseline. FLTrust assigns trust weights to client updates based on their alignment with a small server-held “root” update computed on trusted data, attenuating updates that deviate from this reference [6]. FoolsGold down-weights clients whose updates are consistently similar to each other, targeting sybil-style attackers that submit correlated gradients across identities [12]. MultiKrum averages client updates that are most consistent with the majority by minimizing distances to the nearest neighbors, thereby filtering out outliers under a bounded number of Byzantine clients [5].

Overall, the results show that these robust aggregation schemes do not reliably neutralize temperature-based confidence manipulation. In particular, for FoolsGold and MultiKrum, we observe a pronounced utility collapse (accuracy dropping below $\sim 50\%$ in our setting), indicating that aggressively discarding or down-weighting updates can sacrifice too much benign signal. Despite this degradation, sECE still shifts with τ in the same direction as the undefended baseline, meaning the attack impact on calibration persists while utility deteriorates. In contrast, FLTrust preserves accuracy substantially better than the other robust aggregators, but it still fails to fully prevent confidence steering: the model remains strongly under-confident in the $\tau < 1$ regime (high positive sECE). For $\tau > 1$, FLTrust attenuates the magnitude of over-confidence compared to FedAvg, but the mitigation is partial rather than complete.

Post-hoc calibration. Finally, we evaluate whether post-hoc calibration, where the server or clients recalibrate predictive confidence using a held-out validation set, can mitigate the proposed attack. We consider four representative methods: temperature scaling [17], Platt scaling [45], isotonic regres-

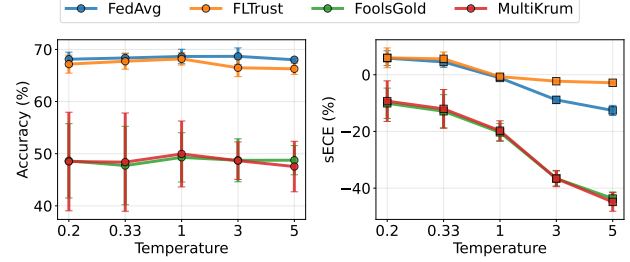


Figure 12: Accuracy and sECE under different aggregation defenses across training temperatures τ .

sion [51], and histogram binning [50]. For each method, we vary the calibration set size from $\{10, 50, 100, 250, 500\}$ samples and measure the resulting sECE.

Figure 13 shows that increasing the number of calibration samples does not reliably neutralize the attack. Except for temperature scaling, the other post-hoc methods exhibit only limited improvement as more samples are available and, in several cases, even amplify signed miscalibration (larger-magnitude sECE). The most effective countermeasure is, somewhat paradoxically, temperature scaling itself; however, it still does not consistently recover clean calibration across attack temperatures. Moreover, in realistic federated deployments with non-IID data, acquiring representative validation data for calibration (and performing calibration repeatedly as the global model evolves) introduces non-trivial overhead and can be challenging in practice. These results suggest that post-hoc calibration alone is insufficient as a robust defense against training-time temperature manipulation.

5.6 Case Study

We now present three case studies to illustrate how the temperature scaling attack can manifest in practical applications and why manipulating calibration is consequential even when top-1 accuracy appears unchanged. We consider (i) mobile healthcare for remote monitoring, (ii) scene understanding in robotics and autonomous driving, and (iii) text generation with language models, where calibrated confidence is directly consumed by downstream decision logic such as alerting, risk control, and selective prediction.

Case #1: Mobile healthcare remote monitoring (risk-triggered triage). Mobile health applications increasingly rely on federated classifiers to detect clinically relevant events (e.g., arrhythmia episodes), where predictive confidence drives operational rules such as “send to clinician if $p(y=\text{abnormal} | x) > \gamma$ ” or “verify low-confidence samples.” Temperature scaling attacks are particularly damaging in such scenarios given that they can shift the probability scale without an obvious accuracy drop, directly corrupting threshold-based triage and resource allocation.

To quantify this effect, we train a 1D-CNN arrhyth-

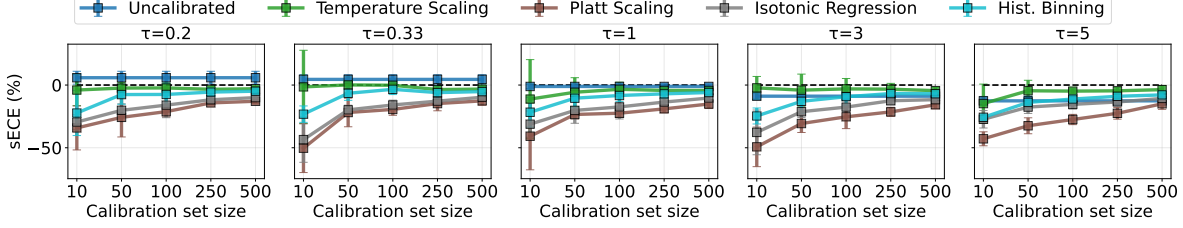


Figure 13: Post-hoc calibration under temperature scaling attacks. We compare four calibration methods as a function of the number of calibration samples, reporting the resulting sECE after calibration.

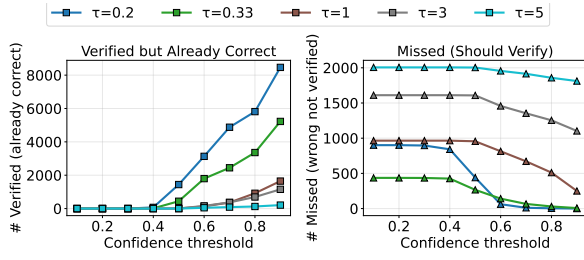


Figure 14: Impact of calibration distortion on threshold-based verification in a mobile healthcare triage workflow. Left: number of *unnecessary* verifications (correct predictions that are still sent for verification). Right: number of *missed* verifications (incorrect predictions that should have been verified but were not), as a function of the confidence threshold γ .

mia classifier with 10 clients on the MIT-BIH arrhythmia database [38] for 20 FL rounds, and assume that samples with confidence below a threshold γ are forwarded to a server/clinician for additional verification. Figure 14 plots two operational costs as γ varies: (i) *Verified but already correct*, i.e., unnecessary verification requests, and (ii) *Missed (should verify)*, i.e., incorrect predictions that bypass verification. Under an under-confidence attack ($\tau < 1$), the model assigns systematically lower confidences, which inflates the verification workload: at $\gamma=0.9$, unnecessary verifications increase from 1,647 ($\tau=1$) to 8,465 ($\tau=0.2$), a +414.0% rise. Conversely, under an over-confidence attack ($\tau > 1$), the model becomes overly certain, causing risky samples to skip verification: at $\gamma=0.9$, missed verifications increase from 250 ($\tau=1$) to 1,812 ($\tau=5$), a +624.8% rise. These results suggest that calibration integrity is safety-critical in risk-triggered workflows, with the primary harm not being significant changes in accuracy, but a large shift in downstream decisions governed by confidence thresholds.

Case #2: Robotics and autonomous driving (selective perception and safety gating). Robots and autonomous vehicles commonly use confidence scores from perception modules (e.g., detection/segmentation) to gate downstream behaviors, such as triggering conservative planning, requesting additional sensing, or initiating a fallback mode when con-

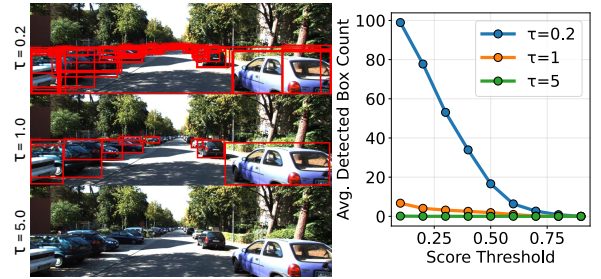


Figure 15: Selective perception under temperature-induced miscalibration in DETR. Left: detections on the same KITTI image at a fixed score threshold (0.3) for $\tau \in \{0.2, 1, 5\}$. Right: average number of retained boxes versus the score threshold. Low τ yields many false positives (too many boxes), while high τ suppresses detections (near-zero boxes).

fidence is low. Temperature-driven miscalibration can systematically bias these gates as over-confidence may suppress fallbacks and pass incorrect outputs to planning, while under-confidence can cause excessive caution or unnecessary interventions. Since these policies react to calibrated confidence rather than accuracy alone, the impact can be disproportionate even when standard validation accuracy appears unchanged.

To emulate this scenario, we fine-tune a COCO2017-pretrained DETR model [7] on the KITTI 2D detection benchmark [15] in a federated manner under three temperatures, $\tau \in \{0.2, 1.0, 5.0\}$. DETR produces 100 object queries and, for each query, estimates a “no-object” probability; a query is kept as a detection only if its no-object score is below a threshold. As a result, the temperature directly alters the effective selectivity of the detector. With low temperature ($\tau < 1$), the no-object probability becomes *under-confident*; thus, many queries are incorrectly treated as objects, leading to a flood of detections. With high temperature ($\tau > 1$), the no-object score becomes *over-confident*, leading to true objects being filtered.

Figure 15 visualizes this failure mode. At the same score threshold (0.3), $\tau=0.2$ produces an excessive number of boxes that can overwhelm downstream tracking and planning, whereas $\tau=5$ can suppress detection altogether, effectively making the system “blind.” The right panel further confirms a systematic shift in the average number of retained boxes

Prompt (Input). Perhaps because Abraham Lincoln had not yet been
$\tau = 1.0$ (baseline). <i>Perhaps because Abraham Lincoln had not yet been inaugurated as President, Captain Totten received no instructions from his superiors.</i>
$\tau = 0.5$ (attacked / under-confident). <i>Perhaps because Abraham Lincoln had not yet been inaugurated as President, not as President the arsenal of Captain Totten was constructed. On January 8, 1861, the state legislature decided a arsenal, but found no citizens to engage in such undertakings A grid @-@@@ person, not as this character. @-@ for @. Note there, then the which'Aotten received in the, construction.</i>

Figure 16: Qualitative example of temperature-controlled generation behavior. Lower temperature ($\tau=0.5$) produces a degraded continuation with repetition, factual drift, and corrupted tokens, compared to the coherent baseline at $\tau=1.0$.

across thresholds. These results showcase how temperature scaling can translate into practical safety and performance risks by corrupting confidence-based gating in real perception pipelines.

Case #3: Federated language models (confidence-based generation control). In federated language modeling, token probabilities are directly consumed by decoding and control logic (e.g., top- p sampling [20], abstention, or retrieval triggers) [47]. Thus, manipulating calibration during training can change generation behavior even with small next-token accuracy changes. In particular, lower temperature ($\tau < 1$) training induces *under-confidence*, yielding a *flatter* predictive distribution at inference; conversely, higher temperatures push the model toward over-confidence and overly peaky posteriors.

We demonstrate this effect with a pretrained GPT-2 [46] fine-tuned on WikiText-2 [37] via FL. Using standard top- p sampling at inference, the attacked model trained with $\tau=0.5$ produces markedly degraded continuations compared to the benign baseline ($\tau=1.0$), including repetition, factual drift, and corrupted tokens (Figure 16). This highlights that training-time temperature manipulation can shift the probability scale that governs decoding, making confidence-based generation pipelines a practical target.

6 Discussion

Calibration Attacks in Federated Learning. We view one of our key contributions as establishing *calibration integrity* as an attack objective in federated learning. While our work introduces a training-time temperature scaling attack, we hope it motivates broader research on stronger attacks and principled defenses. This direction matters since many FL applications consume predictive confidence as an operational signal (e.g., selective prediction, human-in-the-loop review, and resource allocation), and confidence failures can be consequential even

when accuracy appears normal. These trends highlight the need for calibration-aware auditing and protection in FL, beyond conventional monitoring focused on loss or accuracy.

Practical Limitations. Our threat model assumes the attacker can control the local training pipeline, which is common in FL security studies but can be demanding in practice. In cross-device deployments, achieving such control may require elevated capabilities (e.g., rooting/jailbreaking, or bypassing integrity checks), raising attacker cost and expertise requirements. An important next step is to study weaker adversaries that cannot directly modify training, but can manipulate data or labels to approximate similar update behavior (e.g., gradient-matching style objectives). Even under this idealized assumption, our results isolate a core vulnerability: calibration can be manipulated largely independently of accuracy within federated optimization.

Future Work. This work targets *global* calibration manipulation for multi-class classification. A natural extension is *class-targeted* calibration attacks that selectively distort confidence for specific classes while leaving others relatively intact, enabling more fine-grained behaviors. It is also valuable to expand to tasks where uncertainty is directly consumed downstream, such as detection/segmentation (per-instance confidence), sequence prediction and generation (token-level uncertainty), and risk-sensitive decision pipelines. These directions can help characterize the robustness of confidence-aware FL systems and inform task-specific defenses.

7 Conclusion

In this work, we demonstrated that *calibration integrity* is a practical attack target in federated learning. Our *temperature scaling attack* manipulates predictive confidence during local training, steering the global model toward systematic overconfidence or underconfidence while largely preserving accuracy. We analyzed temperature-scaled local SGD in the standard non-convex FL framework and highlighted an effective-step-size invariance: coupling learning rate and temperature via $\beta = \eta/\tau$ yields benign-like optimization behavior up to standard noise and drift terms. Across three benchmarks, the attack induces large, directional calibration shifts, yet remains difficult to flag using common signals such as accuracy trajectories, update-direction similarity, and representation/output similarity measures. These results motivate calibration-aware monitoring and defenses in federated learning.

Ethical Considerations

This paper identifies *calibration integrity* as an attack objective in federated learning and proposes a training-time temperature scaling attack. The primary ethical risk is misuse: an attacker could intentionally induce over-/under-confidence and cause unsafe downstream decisions in applications that

rely on predictive uncertainty (e.g., triage, selective prediction, or human-in-the-loop review).

We mitigate this risk by focusing on responsible disclosure through rigorous characterization rather than deployment guidance. Our contribution is to surface a previously under-studied vulnerability, quantify when it arises, and evaluate representative defenses (robust aggregation and post-hoc calibration), which can help practitioners build calibration-aware auditing and monitoring. We do not use any private data; all experiments use standard public benchmarks and standard models. Overall, we believe the defensive value of understanding and measuring this failure mode outweighs the potential harms, and we encourage future work on practical detection and mitigation of calibration-targeted behaviors in FL.

Open Science

We will release the code to reproduce all results in this paper, including: (i) the temperature scaling attack with η - τ coupling via β , (ii) the FL training/evaluation pipeline, (iii) baseline attacks (noise injection, label flipping), and (iv) evaluated defenses. All datasets and models are public and standard (MNIST, CIFAR-10, CIFAR-100, MITBIH Arrhythmia, KITTI-2D, WikiText2; MLP/CNN/ResNet-18/DETR/GPT-2). We provide an [anonymized repository](#) for reproducibility. While the codebase will be further polished to streamline execution, we will include the repository link and exact run instructions in the final version.

References

- [1] Atish Agarwala, Jeffrey Pennington, Yann Dauphin, and Sam Schoenholz. Temperature check: theory and practice for training models with softmax-cross-entropy losses. *arXiv preprint arXiv:2010.07344*, 2020.
- [2] Pasquale Antonante, Sushant Veer, Karen Leung, Xinshuo Weng, Luca Carlone, and Marco Pavone. Task-aware risk estimation of perception failures for autonomous vehicles. *arXiv preprint arXiv:2305.01870*, 2023.
- [3] Eugene Bagdasaryan, Andreas Veit, Yiqing Hua, Deborah Estrin, and Vitaly Shmatikov. How to backdoor federated learning. In *International conference on artificial intelligence and statistics*, pages 2938–2948. PMLR, 2020.
- [4] Arjun Nitin Bhagoji, Supriyo Chakraborty, Prateek Mittal, and Seraphin Calo. Analyzing federated learning through an adversarial lens. In *International conference on machine learning*, pages 634–643. PMLR, 2019.
- [5] Peva Blanchard, El Mahdi El Mhamdi, Rachid Gueraoui, and Julien Stainer. Machine learning with adversaries: Byzantine tolerant gradient descent. *Advances in neural information processing systems*, 30, 2017.
- [6] Xiaoyu Cao, Minghong Fang, Jia Liu, and Neil Zhenqiang Gong. Fltrust: Byzantine-robust federated learning via trust bootstrapping. *arXiv preprint arXiv:2012.13995*, 2020.
- [7] Nicolas Carion, Francisco Massa, Gabriel Synnaeve, Nicolas Usunier, Alexander Kirillov, and Sergey Zagoruyko. End-to-end object detection with transformers. In *European conference on computer vision*, pages 213–229. Springer, 2020.
- [8] Nicholas Carlini and David Wagner. Towards evaluating the robustness of neural networks. In *2017 ieee symposium on security and privacy (sp)*, pages 39–57. Ieee, 2017.
- [9] Jinqian Chen, Jihua Zhu, Qinghai Zheng, Zhongyu Li, and Zhiqiang Tian. Watch your head: Assembling projection heads to save the reliability of federated models. In *Proceedings of the AAAI Conference on Artificial Intelligence*, volume 38, pages 11329–11337, 2024.
- [10] Kevin Eykholt, Ivan Evtimov, Earlene Fernandes, Bo Li, Amir Rahmati, Chaowei Xiao, Atul Prakash, Tadayoshi Kohno, and Dawn Song. Robust physical-world attacks on deep learning visual classification. In *Proceedings of the IEEE conference on computer vision and pattern recognition*, pages 1625–1634, 2018.
- [11] Minghong Fang, Xiaoyu Cao, Jinyuan Jia, and Neil Gong. Local model poisoning attacks to {Byzantine-Robust} federated learning. In *29th USENIX security symposium (USENIX Security 20)*, pages 1605–1622, 2020.
- [12] Clement Fung, Chris JM Yoon, and Ivan Beschastnikh. Mitigating sybils in federated learning poisoning. *arXiv preprint arXiv:1808.04866*, 2018.
- [13] Ido Galil and Ran El-Yaniv. Disrupting deep uncertainty estimation without harming accuracy. *Advances in Neural Information Processing Systems*, 34:21285–21296, 2021.
- [14] Yonatan Geifman and Ran El-Yaniv. Selective classification for deep neural networks. *Advances in neural information processing systems*, 30, 2017.
- [15] Andreas Geiger, Philip Lenz, and Raquel Urtasun. Are we ready for autonomous driving? the kitti vision benchmark suite. In *Conference on Computer Vision and Pattern Recognition (CVPR)*, 2012.
- [16] Ian J Goodfellow, Jonathon Shlens, and Christian Szegedy. Explaining and harnessing adversarial examples. *arXiv preprint arXiv:1412.6572*, 2014.

[17] Chuan Guo, Geoff Pleiss, Yu Sun, and Kilian Q Weinberger. On calibration of modern neural networks. In *International conference on machine learning*, pages 1321–1330. PMLR, 2017.

[18] Dongfang Guo, Yuting Wu, Yimin Dai, Pengfei Zhou, Xin Lou, and Rui Tan. Invisible optical adversarial stripes on traffic sign against autonomous vehicles. In *Proceedings of the 22nd Annual International Conference on Mobile Systems, Applications and Services*, pages 534–546, 2024.

[19] Geoffrey Hinton, Oriol Vinyals, and Jeff Dean. Distilling the knowledge in a neural network. *arXiv preprint arXiv:1503.02531*, 2015.

[20] Ari Holtzman, Jan Buys, Li Du, Maxwell Forbes, and Yejin Choi. The curious case of neural text degeneration. *arXiv preprint arXiv:1904.09751*, 2019.

[21] Tzu-Ming Harry Hsu, Hang Qi, and Matthew Brown. Measuring the effects of non-identical data distribution for federated visual classification. *arXiv preprint arXiv:1909.06335*, 2019.

[22] Eric Jang, Shixiang Gu, and Ben Poole. Categorical reparameterization with gumbel-softmax. *arXiv preprint arXiv:1611.01144*, 2016.

[23] Alex Kendall and Yarin Gal. What uncertainties do we need in bayesian deep learning for computer vision? *Advances in neural information processing systems*, 30, 2017.

[24] Juyeop Kim, Junha Park, Songkuk Kim, and Jong-Seok Lee. Curved representation space of vision transformers. In *Proceedings of the AAAI Conference on Artificial Intelligence*, volume 38, pages 13142–13150, 2024.

[25] Benjamin Kompa, Jasper Snoek, and Andrew L Beam. Second opinion needed: communicating uncertainty in medical machine learning. *NPJ Digital Medicine*, 4(1):4, 2021.

[26] Alexey Kurakin, Ian J Goodfellow, and Samy Bengio. Adversarial examples in the physical world. In *Artificial intelligence safety and security*, pages 99–112. Chapman and Hall/CRC, 2018.

[27] Emanuele Ledda, Daniele Angioni, Giorgio Piras, Giorgio Fumera, Battista Biggio, and Fabio Roli. Adversarial attacks against uncertainty quantification. In *Proceedings of the IEEE/CVF International Conference on Computer Vision*, pages 4599–4608, 2023.

[28] Joonhee Lee, Hyunseung Shin, and Jeonggil Ko. Iros: A dual-process architecture for real-time vlm-based indoor navigation. *arXiv preprint arXiv:2601.21506*, 2026.

[29] Kichang Lee, Jaeho Jin, JaeYeon Park, Songkuk Kim, and JeongGil Ko. Tazza: Shuffling neural network parameters for secure and private federated learning. *arXiv preprint arXiv:2412.07454*, 2024.

[30] Kichang Lee, Yujin Shin, Jonghyuk Yun, Songkuk Kim, Jun Han, and JeongGil Ko. Detrigger: A gradient-centric approach to backdoor attack mitigation in federated learning. *arXiv preprint arXiv:2411.12220*, 2024.

[31] Kichang Lee, Jonghyuk Yun, Jun Han, and Jeonggil Ko. Exploiting indices for man-in-the-middle attacks on collaborative unpooling autoencoders. In *Proceedings of the 21st Annual International Conference on Mobile Systems, Applications and Services*, pages 598–599, 2023.

[32] Kichang Lee, Jonghyuk Yun, Jaeho Jin, Jun Han, and Jeonggil Ko. Mind your indices! index hijacking attacks on collaborative unpooling autoencoder systems. *Internet of Things*, 29:101462, 2025.

[33] Kichang Lee, Pei Zhang, Songkuk Kim, and JeongGil Ko. Improving local training in federated learning via temperature scaling. *Advanced Engineering Informatics*, 71:104283, 2026.

[34] Lingjuan Lyu, Han Yu, Xingjun Ma, Chen Chen, Lichao Sun, Jun Zhao, Qiang Yang, and Philip S Yu. Privacy and robustness in federated learning: Attacks and defenses. *IEEE transactions on neural networks and learning systems*, 35(7):8726–8746, 2022.

[35] Aleksander Madry, Aleksandar Makelov, Ludwig Schmidt, Dimitris Tsipras, and Adrian Vladu. Towards deep learning models resistant to adversarial attacks. *arXiv preprint arXiv:1706.06083*, 2017.

[36] Brendan McMahan, Eider Moore, Daniel Ramage, Seth Hampson, and Blaise Aguera y Arcas. Communication-efficient learning of deep networks from decentralized data. In *Artificial intelligence and statistics*, pages 1273–1282. PMLR, 2017.

[37] Stephen Merity, Caiming Xiong, James Bradbury, and Richard Socher. Pointer sentinel mixture models, 2016.

[38] George B Moody and Roger G Mark. The impact of the mit-bih arrhythmia database. *IEEE engineering in medicine and biology magazine*, 20(3):45–50, 2001.

[39] Thien Duc Nguyen, Phillip Rieger, Huili Chen, Hossein Yalame, Helen Möllering, Hossein Fereidooni, Samuel Marchal, Markus Miettinen, Azalia Mirhoseini, Shaza Zeitouni, et al. {FLAME}: Taming backdoors in federated learning. In *31st USENIX Security Symposium (USENIX Security 22)*, pages 1415–1432, 2022.

[40] Alexandru Niculescu-Mizil and Rich Caruana. Predicting good probabilities with supervised learning. In *Proceedings of the 22nd international conference on Machine learning*, pages 625–632, 2005.

[41] Stephen Obadinma, Xiaodan Zhu, and Hongyu Guo. Calibration attacks: A comprehensive study of adversarial attacks on model confidence. *arXiv preprint arXiv:2401.02718*, 2024.

[42] Jaeyeon Park, Hyeyon Cho, Rajesh Krishna Balan, and JeongGil Ko. Heartquake: Accurate low-cost non-invasive ecg monitoring using bed-mounted geophones. *Proceedings of the ACM on Interactive, Mobile, Wearable and Ubiquitous Technologies*, 4(3):1–28, 2020.

[43] JaeYeon Park, Kichang Lee, Noseong Park, Seng Chan You, and JeongGil Ko. Self-attention lstm-fcn model for arrhythmia classification and uncertainty assessment. *Artificial Intelligence in Medicine*, 142:102570, 2023.

[44] Hongyi Peng, Han Yu, Xiaoli Tang, and Xiaoxiao Li. Fedcal: Achieving local and global calibration in federated learning via aggregated parameterized scalar. *arXiv preprint arXiv:2405.15458*, 2024.

[45] John Platt et al. Probabilistic outputs for support vector machines and comparisons to regularized likelihood methods. *Advances in large margin classifiers*, 10(3):61–74, 1999.

[46] Alec Radford, Jeffrey Wu, Rewon Child, David Luan, Dario Amodei, Ilya Sutskever, et al. Language models are unsupervised multitask learners. *OpenAI blog*, 1(8):9, 2019.

[47] Lorenzo Sani, Alex Iacob, Zeyu Cao, Royson Lee, Bill Marino, Yan Gao, Wanru Zhao, Dongqi Cai, Zexi Li, Xinchi Qiu, et al. Photon: Federated llm pre-training. *Proceedings of Machine Learning and Systems*, 7, 2025.

[48] Chulin Xie, Keli Huang, Pin-Yu Chen, and Bo Li. Dba: Distributed backdoor attacks against federated learning. In *International conference on learning representations*, 2019.

[49] Dong Yin, Yudong Chen, Ramchandran Kannan, and Peter Bartlett. Byzantine-robust distributed learning: Towards optimal statistical rates. In *International conference on machine learning*, pages 5650–5659. Pmlr, 2018.

[50] Bianca Zadrozny and Charles Elkan. Obtaining calibrated probability estimates from decision trees and naive bayesian classifiers. In *Icml*, volume 1, 2001.

[51] Bianca Zadrozny and Charles Elkan. Transforming classifier scores into accurate multiclass probability estimates. In *Proceedings of the eighth ACM SIGKDD international conference on Knowledge discovery and data mining*, pages 694–699, 2002.

[52] Shimao Zhang, Yu Bao, and Shujian Huang. Edt: Improving large language models’ generation by entropy-based dynamic temperature sampling. *arXiv preprint arXiv:2403.14541*, 2024.

[53] Fei Zhu, Zhen Cheng, Xu-Yao Zhang, and Cheng-Lin Liu. Rethinking confidence calibration for failure prediction. In *European conference on computer vision*, pages 518–536. Springer, 2022.

[54] Yuqi Zhu, Jia Li, Ge Li, YunFei Zhao, Zhi Jin, and Hong Mei. Hot or cold? adaptive temperature sampling for code generation with large language models. In *Proceedings of the AAAI Conference on Artificial Intelligence*, volume 38, pages 437–445, 2024.

A Additional Theoretical Details

A.1 Proof sketch for Lemma 1

Proof sketch. We formalize how temperature enters the curvature of the softmax cross-entropy objective. Consider a single example (x, y) , logits $\mathbf{z}(\theta; x) \in \mathbb{R}^K$, and the temperature-scaled predictive distribution

$$\mathbf{p}_\tau \triangleq \text{softmax}(\mathbf{z}(\theta; x)/\tau).$$

Let $\ell_\tau(\theta; x, y)$ denote the cross-entropy loss computed with \mathbf{p}_τ . Now, we decompose the Hessian w.r.t. parameters via the multivariate chain rule. Writing ℓ_τ as a composition $\ell_\tau(\theta; x, y) = \tilde{\ell}_\tau(\mathbf{z}(\theta; x), y)$, we obtain

$$\nabla_\theta^2 \ell_\tau = \underbrace{(\mathbf{J}_\theta \mathbf{z})^\top (\nabla_\mathbf{z}^2 \tilde{\ell}_\tau) (\mathbf{J}_\theta \mathbf{z})}_{\text{Term (A)}} + \underbrace{\sum_{i=1}^K \frac{\partial \tilde{\ell}_\tau}{\partial z_i} \nabla_\theta^2 z_i}_{\text{Term (B)}} \quad (14)$$

Term (A): First-order interaction.

For softmax cross-entropy, the Hessian w.r.t. logits is

$$\nabla_\mathbf{z}^2 \tilde{\ell}_\tau = \frac{1}{\tau^2} \left(\text{diag}(\mathbf{p}_\tau) - \mathbf{p}_\tau \mathbf{p}_\tau^\top \right). \quad (15)$$

The matrix $\text{diag}(\mathbf{p}_\tau) - \mathbf{p}_\tau \mathbf{p}_\tau^\top$ is the covariance of a categorical distribution and has operator norm at most $1/4$. Hence

$$\|\nabla_\mathbf{z}^2 \tilde{\ell}_\tau\| \leq \frac{1}{4\tau^2}. \quad (16)$$

Using the Jacobian bound $\|\mathbf{J}_\theta \mathbf{z}(\theta; x)\| \leq G(x)$, we can upper bound Term (A) as

$$\|(\mathbf{J}_\theta \mathbf{z})^\top (\nabla_\mathbf{z}^2 \tilde{\ell}_\tau) (\mathbf{J}_\theta \mathbf{z})\| \leq \|\mathbf{J}_\theta \mathbf{z}\|^2 \cdot \|\nabla_\mathbf{z}^2 \tilde{\ell}_\tau\| \leq \frac{G(x)^2}{4\tau^2}, \quad (17)$$

which exhibits the strict $1/\tau^2$ scaling.

Term (B): Logit curvature effect.

The gradient of softmax cross-entropy w.r.t. logits satisfies

$$\frac{\partial \tilde{\ell}_\tau}{\partial z_i} = \frac{1}{\tau} (p_{i,\tau} - \mathbb{1}[i=y]), \quad (18)$$

and thus its magnitude is suppressed by $1/\tau$. Therefore, the second term in (14) is also attenuated by temperature:

$$\left\| \sum_{i=1}^K \frac{\partial \tilde{\ell}_\tau}{\partial z_i} \nabla_{\theta}^2 z_i \right\| \leq \frac{1}{\tau} \sum_{i=1}^K |p_{i,\tau} - \mathbb{1}[i=y]| \cdot \|\nabla_{\theta}^2 z_i\|. \quad (19)$$

In common deep architectures, $\nabla_{\theta}^2 z_i$ is often small in spectral norm compared to the Jacobian-mediated term, and Term (A) typically dominates the Hessian spectrum. Under this regime, the overall curvature inherits the $O(1/\tau^2)$ behavior. More generally, one may absorb Term (B) into $C(x)$ by assuming a bounded logit curvature condition, for example $\sum_{i=1}^K \|\nabla_{\theta}^2 z_i\| \leq H(x)$, which yields

$$\left\| \sum_{i=1}^K \frac{\partial \tilde{\ell}_\tau}{\partial z_i} \nabla_{\theta}^2 z_i \right\| \leq \frac{2H(x)}{\tau}, \quad (20)$$

and the overall bound in (12) follows by choosing $C(x)$ to dominate both terms (e.g., for $\tau \geq 1$, the $1/\tau^2$ term is dominant; otherwise $C(x)$ can be defined to cover the worst case over $\tau \in [\tau_{\min}, \tau_{\max}]$).

Combining the bounds for Term (A) and Term (B) establishes (12). Finally, taking expectation over (x, y) yields that the population objective is L_τ -smooth with $L_\tau \leq \bar{C}/\tau^2$ for $\bar{C} = \mathbb{E}[C(x)]$. This temperature-dependent smoothness provides a mathematical basis for the effective step-size invariance $\beta = \eta/\tau$: increasing τ reduces curvature approximately as $1/\tau^2$, so scaling η proportionally to τ preserves (and can even improve) the optimization stability condition through $\eta L_\tau \approx \beta \bar{C}/\tau$.

A.2 Proof sketch for Theorem 1

We outline the standard non-convex argument and highlight where temperature enters the bound. Let θ_t denote the global model at round t , and define the aggregated update $\Delta_t \triangleq \theta_{t+1} - \theta_t$, which is obtained by averaging the local model changes from the M selected clients after E local SGD steps.

Step 1: Descent lemma from L -smoothness. Since F is L -smooth (Assumption 1), for any update Δ_t we have

$$F(\theta_{t+1}) \leq F(\theta_t) + \langle \nabla F(\theta_t), \Delta_t \rangle + \frac{L}{2} \|\Delta_t\|^2. \quad (21)$$

Taking expectation over the randomness of client sampling and mini-batches reduces the analysis to controlling the two terms $\langle \nabla F(\theta_t), \mathbb{E}[\Delta_t] \rangle$ and $\mathbb{E}[\|\Delta_t\|^2]$.

Step 2: Effective step size β and temperature cancellation. Let $\theta_{k,t,e}$ be the local model of client k at local step e within round t with $\theta_{k,t,0} = \theta_t$. The local SGD update takes the form

$$\theta_{k,t,e+1} = \theta_{k,t,e} - \eta_k \mathbf{g}_{k,\tau_k}(\theta_{k,t,e}; \xi_{k,t,e}), \quad (22)$$

where \mathbf{g}_{k,τ_k} is a stochastic gradient computed using the temperature-scaled loss ℓ_{τ_k} . Lemma 1 implies that the temperature-scaled gradient is approximately rescaled by $1/\tau_k$ (relative to the $\tau=1$ loss), i.e., $\nabla \ell_{\tau_k} \approx \frac{1}{\tau_k} \nabla \ell$. Combining this with Assumption 4 ($\eta_k = \beta \tau_k$) yields the effective update

$$\eta_k \nabla \ell_{\tau_k} \approx (\beta \tau_k) \left(\frac{1}{\tau_k} \nabla \ell \right) = \beta \nabla \ell, \quad (23)$$

so all participating clients move with a common effective step size β despite heterogeneous (η_k, τ_k) . Consequently, the aggregated update can be written as

$$\begin{aligned} \Delta_t &= \frac{1}{M} \sum_{k \in \mathcal{K}} (\theta_{k,t,E} - \theta_t) \\ &= -\frac{1}{M} \sum_{k \in \mathcal{K}} \sum_{e=0}^{E-1} \eta_k \mathbf{g}_{k,\tau_k}(\theta_{k,t,e}; \xi_{k,t,e}), \end{aligned} \quad (24)$$

and its conditional expectation satisfies (up to the approximation in (23))

$$\mathbb{E}[\Delta_t | \theta_t] \approx -\beta \cdot \frac{1}{M} \sum_{k \in \mathcal{K}} \sum_{e=0}^{E-1} \mathbb{E}[\nabla f_k(\theta_{k,t,e}) | \theta_t]. \quad (25)$$

Step 3: Descent term and client drift. Substituting (25) into the inner-product term in (21) gives

$$\begin{aligned} &\left\langle \nabla F(\theta_t), \mathbb{E}[\Delta_t | \theta_t] \right\rangle \\ &\approx -\beta \sum_{e=0}^{E-1} \left\langle \nabla F(\theta_t), \frac{1}{M} \sum_{k \in \mathcal{K}} \mathbb{E}[\nabla f_k(\theta_{k,t,e}) | \theta_t] \right\rangle \\ &= -\beta E \|\nabla F(\theta_t)\|^2 + \text{Drift}_t, \end{aligned} \quad (26)$$

where Drift_t collects the deviation between the local gradients evaluated at $\theta_{k,t,e}$ and the global gradient at θ_t . Bounding Drift_t is the main technical step in non-convex FL analyses; using Assumption 3 and standard arguments that control $\|\theta_{k,t,e} - \theta_t\|$ across E local steps yields a drift contribution of order $O(\beta^2 L^2 E^2 \Gamma^2)$ in the final bound.

Step 4: Bounding the quadratic term via variance and heterogeneity. The term $\mathbb{E}[\|\Delta_t\|^2]$ in (21) is bounded using Assumption 2 (stochastic gradient noise) and Assumption 3 (gradient dissimilarity across clients). This yields a contribution of order $O(\beta^2 E \sigma^2 / M)$ from stochastic variance and an additional heterogeneity-dependent term that is absorbed

into the drift term above. Collecting terms and simplifying constants gives a one-round recursion of the form

$$\begin{aligned} \mathbb{E}[F(\theta_{t+1})] &\leq \mathbb{E}[F(\theta_t)] - \frac{\beta E}{2} \mathbb{E}[\|\nabla F(\theta_t)\|^2] \\ &\quad + O\left(\frac{\beta^2 L E \sigma^2}{M}\right) + O(\beta^3 L^2 E^3 \Gamma^2). \end{aligned} \quad (27)$$

where we omit lower-order terms and adjust constants for readability.

Step 5: Telescoping over rounds. Summing (27) over $t = 0, \dots, T-1$ yields a telescoping left-hand side $\mathbb{E}[F(\theta_T) - F(\theta_0)] \geq F^* - F(\theta_0)$. Rearranging and dividing by βET results in

$$\begin{aligned} \frac{1}{T} \sum_{t=0}^{T-1} \mathbb{E}[\|\nabla F(\theta_t)\|^2] &\leq \frac{2(F(\theta_0) - F^*)}{\beta ET} \\ &\quad + O\left(\frac{\beta L \sigma^2}{M}\right) + O(\beta^2 L^2 E^2 \Gamma^2), \end{aligned} \quad (28)$$

which matches Eq. (13) up to constants. This derivation formalizes that maintaining a benign-range effective step size β is sufficient to preserve a benign-like convergence profile, even when clients employ heterogeneous temperatures during local training.

Bridging local scaling to global convergence. The connection between temperature-scaled local updates and the global convergence bound in Eq. (13) relies on the substitution of the constant effective step size β . By substituting $\eta_k = \beta \tau_k$ into the local update $\theta_{t,e+1} = \theta_{t,e} - \eta_k \nabla \ell_{\tau_k}(\theta_{t,e})$, and noting that $\nabla \ell_{\tau_k} \approx \frac{1}{\tau_k} \nabla \ell$ (where ℓ is the unscaled loss), the update becomes:

$$\begin{aligned} \theta_{t,e+1} &\approx \theta_{t,e} - (\beta \tau_k) \left(\frac{1}{\tau_k} \nabla \ell(\theta_{t,e}) \right) \\ &= \theta_{t,e} - \beta \nabla \ell(\theta_{t,e}). \end{aligned} \quad (29)$$

This cancellation effectively removes the explicit dependence on τ_k from the primary descent term in the global analysis. Consequently, the resulting model updates Δ_t follow a trajectory consistent with benign training under step size β and base smoothness L , making the attack difficult to detect through global convergence diagnostics while systematically altering predictive confidence.

B Experimental Details

B.1 Federated learning setup

This appendix provides implementation and protocol details to facilitate reproducibility. Unless otherwise specified, we use synchronous cross-device FL with FedAvg as summarized

Configuration	MNIST	CIFAR10	CIFAR100
# Clients (K)	50		
Clients / round (M)	5 (10%)		
Attacker ratio	25% (13/50)		
Dirichlet α	1.0		
Optimizer	SGD		
Model architecture	MLP	CNN	ResNet18
Effective step (β)	0.01	0.05	0.05
Batch size	64		
Total rounds	100		
Local steps (E)	5		
Random seeds	{0,1,2,3,4}		

Table 4: Federated learning and attack configuration across dataset–model pairs (default settings unless stated otherwise).

Configuration	Case #1	Case #2	Case #3
Dataset	MITBIH	KITTI-2D	WikiText2
Model architecture	1D CNN	DETR	GPT-2
Pretraining	✗	✓	✓
# Clients (K)	20	10	10
Clients / round (M)		5	
Attacker ratio		25%	
Optimizer	SGD		AdamW
Effective step (β)	0.01	1e-4	2e-3
Batch size		64	
Total rounds		20	
Local steps (E)		5	

Table 5: Configuration used for case studies in Section 5.6.

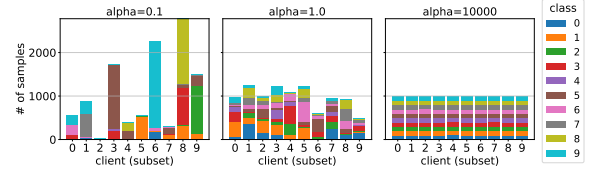


Figure 17: Example client label distributions under Dirichlet partitioning for CIFAR-10 with different concentration parameters α (smaller α yields more heterogeneous splits).

in Table 4. We instantiate $K = 50$ total clients and sample $M = 5$ clients (10%) uniformly at random per round. Each selected client performs $E = 5$ steps of local SGD on its private data and sends model updates back to the server, which aggregates using data-size weights p_k .

Non-IID partitioning. To model statistical heterogeneity, we partition each dataset across clients using a Dirichlet split [21]. Specifically, for each class c , we draw a client-wise proportion vector $\pi_c \sim \text{Dirichlet}(\alpha)$ and allocate samples of class c to clients according to π_c . The concentration parameter α controls the non-IID severity: smaller α yields more skewed, label-dominant clients, while larger α approaches an

approximately IID split. Figure 17 visualizes representative label distributions under different α . As shown, the data distribution emulates both the quantity and label heterogeneity. Unless otherwise specified, we use $\alpha = 1.0$, and we sweep α in our sensitivity experiments (Fig. 10).

In addition, for the case studies in Section 5.6, we use different experiment configuration as shown in Table 5.

B.2 Centered Kernel Alignment

Centered Kernel Alignment (CKA) is a similarity measure between two sets of representations that compares their *pairwise relational structure* rather than individual coordinates. Given two feature matrices $X \in \mathbb{R}^{n \times d_x}$ and $Y \in \mathbb{R}^{n \times d_y}$ extracted from the same n inputs, CKA measures how similarly X and Y represent the input set.

Direct cosine similarity between high-dimensional features is often brittle because it depends on the particular basis of the representation space. In contrast, CKA is invariant to orthogonal transformations of the features (e.g., rotations) and is robust to feature reparameterizations that preserve representational structure. This makes CKA well-suited for comparing penultimate-layer features across independently trained models, where equivalent representations may differ by a rotation or other benign reparameterizations.

In this work, we use *linear* CKA, which is efficient and widely used for neural representation comparison. Let \tilde{X} and \tilde{Y} denote column-centered features (i.e., each feature dimension has zero mean over the n samples). Linear CKA is defined as

$$\text{CKA}(X, Y) \triangleq \frac{\|\tilde{X}^\top \tilde{Y}\|_F^2}{\|\tilde{X}^\top \tilde{X}\|_F \|\tilde{Y}^\top \tilde{Y}\|_F}. \quad (30)$$

Equivalently, linear CKA can be interpreted as the cosine similarity between the (vectorized) centered Gram matrices $\tilde{X} \tilde{X}^\top$ and $\tilde{Y} \tilde{Y}^\top$. In our representation-space analysis, we compute CKA on penultimate-layer activations using a shared evaluation set, so that differences reflect representation drift rather than differences in input distribution.

B.3 Defenses and post-hoc calibration

We evaluate representative robust aggregation rules (FedAvg, FLTrust, FoolsGold, MultiKrum) in Sec. 5.5. When a defense introduces additional hyperparameters, we follow the authors' recommended settings and keep them fixed across temperatures so that the only varying factor is τ .

- **Robust aggregation defenses.** **FedAvg** [36] is the standard baseline that aggregates client updates by data-size weights and performs no explicit adversary filtering. **FLTrust** [6] assigns *trust scores* to client updates using a small server-held trusted dataset. Concretely, the server computes a reference update on the trusted data and reweights each client update by its cosine similarity to the reference direction (often with additional norm clipping), suppressing up-

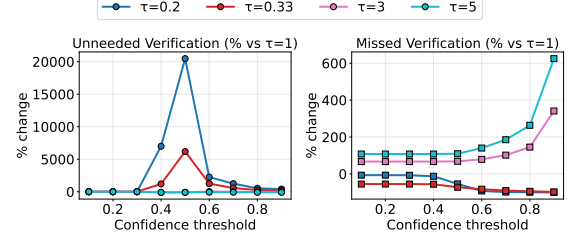


Figure 18: Impact of calibration distortion on threshold-based verification in mobile healthcare triage in percentage change (%). Left: *unnecessary* verifications. Right: *missed* verifications, versus threshold γ .

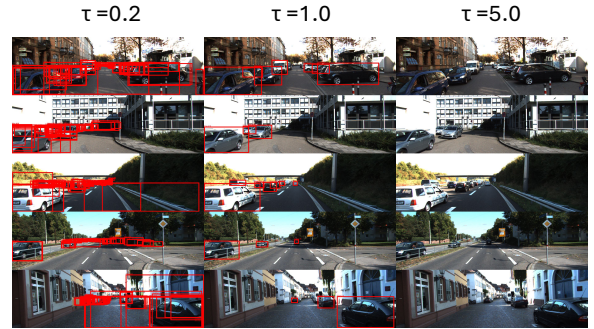


Figure 19: Extended results for selective perception under temperature-induced miscalibration in DETR.

dates that are poorly aligned with the trusted gradient. **FoolsGold** [12] targets sybil-style poisoning by downweighting clients whose updates are *too similar* to others over time. It maintains per-client similarity statistics and reduces the aggregation weight of clients that repeatedly submit highly correlated update directions, under the intuition that colluding attackers tend to produce clustered gradients. **MultiKrum** [5] is a distance-based Byzantine-robust rule. For each client update, it computes the sum of distances to its closest neighbors and selects one or several updates with the smallest such score (i.e., those most consistent with the majority), then aggregates the selected set. This aims to filter out outliers that deviate strongly in update space. • **Post-hoc calibration methods.** For post-hoc calibration (Fig. 13), we evaluate temperature scaling [17], Platt scaling [45], isotonic regression [51], and histogram binning [50]. All methods fit a mapping from an uncalibrated model score to a calibrated confidence using a held-out calibration set. **Temperature scaling** [17] fits a single scalar $T > 0$ that rescales logits at inference, $\mathbf{p} = \text{softmax}(\mathbf{z}/T)$, by minimizing negative log-likelihood on the calibration set. It preserves the predicted class (logit ordering) and only adjusts probability sharpness. **Platt scaling** [45] fits a parametric sigmoid mapping (typically on a scalar score such as a logit margin), $p(y=1 | s) = \sigma(as + b)$, via maximum likelihood on the calibration set. It is a two-parameter, mono-

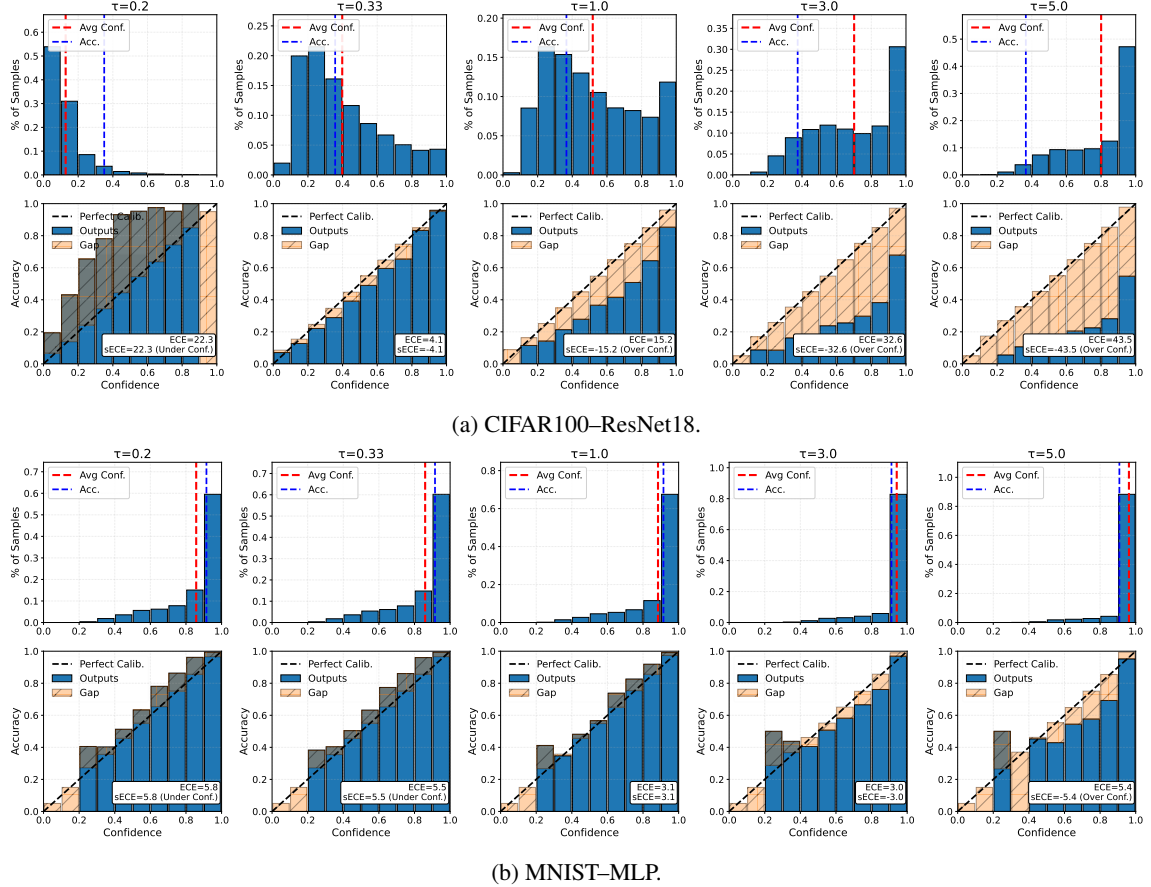


Figure 20: Additional confidence histograms and reliability diagrams under different training temperatures τ . Across both settings, varying τ consistently shifts the confidence distribution and reliability curve while leaving accuracy largely stable.

tone calibrator. **Isotonic regression** [51] fits a non-parametric *monotone* piecewise-constant function that maps scores to probabilities by minimizing squared error subject to monotonicity. It is flexible but can overfit when the calibration set is small. **Histogram binning** [50] partitions scores into bins and replaces each score by the empirical accuracy within its bin. This provides a simple non-parametric estimate of $P(\text{correct} | s)$, with a bias–variance trade-off controlled by the number of bins and calibration-set size.

C Additional Experimental Results

Extended threshold-based triage analysis. Figure 18 extends the mobile healthcare case study by plotting threshold-sweep behavior in percentage form. Using the same verification policy, we report how calibration distortion changes the rate of unnecessary verifications and missed verifications across confidence thresholds γ , illustrating the operational impact of under-/over-confidence beyond a single threshold.

Additional Results for Robotics and Autonomous Driving (selective perception and safety gating). Figure 19 ex-

tends the DETR case study by reporting additional qualitative examples and summary statistics under different training temperatures. The results highlight how temperature-induced miscalibration shifts the confidence of the “no-object” class and, under a fixed score threshold, can lead to systematically different detection behaviors.

Additional reliability diagrams. Figure 20a reports the same confidence histograms and reliability diagrams as in Fig. 2, but for the CIFAR100–ResNet18 configuration (Seed 0). This serves as an additional qualitative check that the temperature-controlled calibration drift (under-/over-confidence as τ varies) persists in a harder, more miscalibrated regime.

Figure 20b provides the corresponding visualization for MNIST–MLP (Seed 0). Although the task is simpler, the same pattern holds: changing the training temperature shifts the confidence distribution and the reliability curve in a consistent direction while leaving accuracy largely stable.